Quaternary Science Reviews 28 (2009) 1037–1054

Contents lists available at ScienceDirect

Quaternary Science Reviews

journal homepage: www.elsevier.com/locate/quascirev

Nature and timing of large landslides in the Himalaya and Transhimalaya of northern India

Jason M. Dortch[a,*], Lewis A. Owen[a], William C. Haneberg[b], Marc W. Caffee[c], Craig Dietsch[a], Ulrich Kamp[d]

[a] Department of Geology, University of Cincinnati, Cincinnati, OH 45221, USA
[b] Haneberg Geoscience, 10208 39th Avenue SW, Seattle WA 98146, USA
[c] Department of Physics/PRIME Laboratory, Purdue University, West Lafayette, IN 47906, USA
[d] Department of Geography, The University of Montana, Missoula, MT 59812, USA

ARTICLE INFO

Article history:
Received 7 January 2008
Received in revised form 18 April 2008
Accepted 5 May 2008

ABSTRACT

Four large landslides, each with a debris volume $>10^6$ m^3, in the Himalaya and Transhimalaya of northern India were examined, mapped, and dated using ^{10}Be terrestrial cosmogenic radionuclide surface exposure dating. The landslides date to 7.7±1.0 ka (Darcha), 7.9±0.8 ka (Patseo), 6.6±0.4 ka (Kelang Serai), and 8.5±0.5 ka (Chilam). Comparison of slip surface dips and physically reasonable angles of internal friction suggests that the landslides may have been triggered by increased pore water pressure, seismic shaking, or a combination of these two processes. However, the steepness of discontinuities in the Darcha rock-slope, suggests that it was more likely to have started as a consequence of gravitationally-induced buckling of planar slabs. Deglaciation of the region occurred more than 2000 years before the Darcha, Patseo, and Kelang Serai landslides; it is unlikely that glacial debuttressing was responsible for triggering the landslides. The four landslides, their causes, potential triggers and mechanisms, and their ages are compared to 12 previously dated large landslides in the region. Fourteen of the 16 dated landslides occurred during periods of intensified monsoons. Seismic shaking, however, cannot be ruled out as a mechanism for landslide initiation, because the Himalaya has experienced great earthquakes on centennial to millennial timescales. The average Holocene landscape lowering due to large landslides for the Lahul region, which contains the Darcha, Patseo, and Kelang Serai landslides, is ~0.12 mm/yr. Previously published large-landslide landscape-lowering rates for the Himalaya differ significantly. Furthermore, regional glacial and fluvial denudation rates for the Himalaya are more than an order of magnitude greater. This difference highlights the lack of large-landslide data, lack of chronology, problems associated with single catchment/large landslide-based calculations, and the need for regional landscape-lowering determinations over a standardized time period.

1. Introduction

Fluvial, glacial, and mass movement processes modify topography, limit slope angles, and produce or destroy relief in the Himalaya (Gilchrist et al., 1994; Zeitler et al., 2001; Spotila et al., 2004). Of these, mass movement is the least well defined in terms of magnitude, age, recurrence, and contribution to overall mountain denudation (Korup et al., 2007; Mitchell et al., 2007), and it can involve very large events. Mass movement has been suggested to be one of the most significant large-scale and long-term processes in the denudation of mountainous regions (Weidinger et al., in press). Korup et al. (2006, 2007) define "large" and "giant" landslides as those producing $>10^6$ m^3 and $>10^8$ m^3 debris, respectively. We use 'large" to describe both large and giant landslides, that is, those with debris volumes $>10^6$ m^3.

As slope angle increases, mass movement processes can dominate slope denudation, and be comparable to fluvial incision rates (Gilchrist et al., 1994). Korup et al. (2007) showed that two-thirds of rock avalanches, from a sample of 300, occurred on the steepest 5% of Earth's surface. The abundance of large landslides in the Himalaya is well illustrated by several studies at the western end of the orogen (Hewitt, 1988, 1998, 1999; Owen, 1991; Owen et al., 1995, 1996; Shroder, 1998; Korup et al., 2007). This suggests that mass movement is one of the most important agents in shaping Himalayan landscapes.

There is much debate regarding the relative importance of high magnitude–low frequency landslides (the large landslides) and low magnitude–high frequency landslides in landscape development.

* Corresponding author.
E-mail address: Dortchjm@uc.edu (J.M. Dortch).

0277-3791/$ – see front matter © 2008 Elsevier Ltd. All rights reserved.
doi:10.1016/j.quascirev.2008.05.002

Identifying, measuring, and dating large landslides enables first-order estimates of mountain denudation due to large-scale mass movements, which can be and compared to denudation due to fluvial and glacial erosion. We focus on large landslides because they have a high potential of preservation and because it is difficult to account for the volumes of thousands of small ones (Dunning et al., 2007). Denudation estimates presented here will be minima, as large-landslide deposits may remain unidentified or may be misidentified, eroded, or reworked.

Causes of large landslides include uplift combined with fluvial or glacial undercutting and slope over-steepening, heavy precipitation, snowmelt, and favorably oriented rock mass discontinuities, sedimentary layering, joints, faults, or schistosity (Korup et al., 2007). The nature of large-landslide triggers, however, is not well understood. The most likely triggers are seismic shaking and intense monsoon precipitation events (Barnard et al., 2001). Co-seismic landsliding has been suggested to occur frequently in tectonically active mountain belts (Keefer, 1994). Bookhagen et al. (2005) suggested, however, that intense monsoon activity may be more significant than earthquakes in triggering large landslides.

Many mass movement deposits throughout the Himalaya and Tibet have been misidentified as glacial deposits (for discussion see Derbyshire, 1983, 1996; Fort, 1986, 1988, 1989, 1995, 1996; Fort and Derbyshire, 1988; Derbyshire and Owen, 1990, 1997; Hewitt, 1999; Benn and Owen, 2002). Extreme fluvial and glacial erosion commonly destroys the diagnostic morphologies of glacial and mass movement landforms, making their identification difficult. Furthermore, the original diamictons that constitute mass movement and glacial deposits are already similar, which can lead to erroneous glacial reconstructions and an incorrect diagnosis of the geomorphic importance of landsliding. Providing accurate descriptions of large-landslide deposits is, therefore, important to help in the accurate reconstruction of glaciation in the Himalaya and Tibet, and for accurately assessing the importance of landslides in landscape evolution.

Few studies have identified, described, measured, and dated large landslides. Detailed studies are needed within and between regions where active erosional and tectonic processes and high relief create favorable condition for large landslides to occur. The Indian Himalaya provides such a geologic and geomorphic setting and allow for inter-regional comparisons, particularly because many studies have already been undertaken across the orogen (Fort et al., 1989; Weidinger et al., 1996; Walder and O'Connor, 1997; Barnard et al., 2001; Bookhagen et al., 2005; Phartiyal et al., 2005; Weidinger, 2006; Mitchell et al., 2007; Weidinger and Korup., in press) (Fig. 1). Furthermore, the many detailed studies of landslides over this large geographic area enable the volume of eroded material generated by landslides to be estimated (Owen et al., 1996; Barnard et al., 2001; Mitchell et al., 2007).

This paper focuses on the nature, timing and importance of large landslides in the landscape evolution of the Himalaya. Using previously published and new data, we summarize large landslides of known age in the Indian Himalaya. We focus on four large landslides, in each case: estimating the volume of the deposit; determining its age using ^{10}Be terrestrial cosmogenic radionuclide surface exposure dating; and discussing possible causes and triggering mechanisms (Fig. 1). We compare these four landslides to other large landslides of known age in the region to explore possible temporal correlations.

2. Regional setting

The study area is located in Lahul (northern Himachal Pradesh) and in Ladakh (in eastern Jammu and Kashmir) between the South Tibetan Detachment Zone and the Karakoram Fault (Yin and Harrison, 2000) (Fig. 1). This seismically active region is composed predominantly of Paleozoic to Cretaceous sedimentary and metasedimentary rocks, granitic intrusions and, north of the Indus River valley, intermediate intrusive rocks of the Ladakh Batholith (Steck, 2003). Specifically, the Phe, Thaple, Muth quartzites, and Lipak Formations are folded, have steeply dipping bedding planes and some discordant granitic intrusions that create rock-slopes susceptible to landsliding (Fuchs and Linner, 1995; Weidinger et al., 2002).

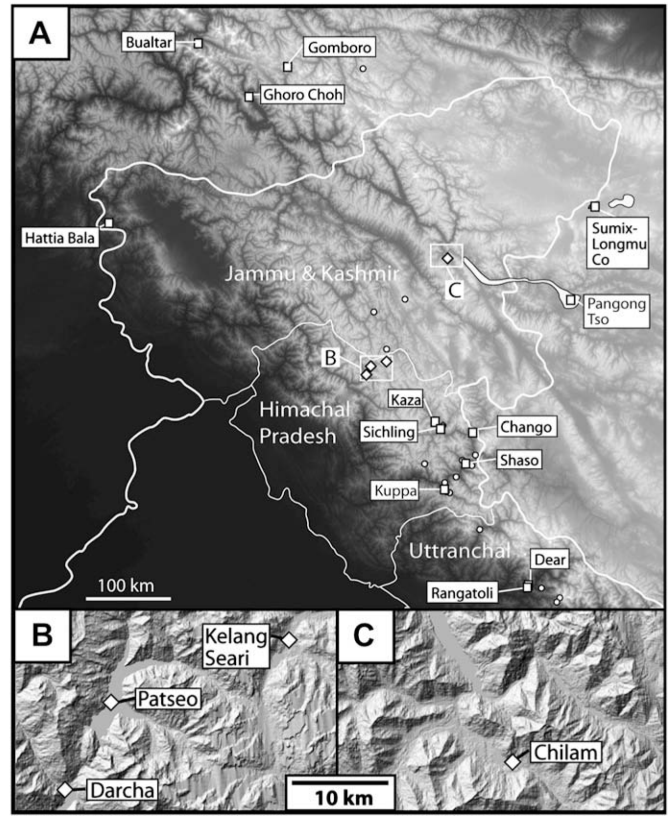

Fig. 1. Locations of landslides investigated for this study (diamonds), landslides with previously published numerical ages (squares), and previously published undated landslides (dots) (data from Hewitt, 1988; Gasse et al., 1996; Barnard et al., 2001, 2004, 2006; Brown et al., 2003; Bookhagen et al., 2005; Dunning et al., 2007; Mitchell et al., 2007; and Seong et al., 2008). (A) SRTM DEM of northern India showing main provinces, topography, and lakes. (B) and (C) ASTER DEMs of the detailed study areas showing the location of the landslide case studies examined in this paper. Abbreviations: T, terrace; DF, debris flow.

The ranges of the Greater Himalaya more than 4500 m above sea level (asl), keep most summer monsoon circulation from reaching the study area (Bookhagen et al., 2005). In spite of this, the monsoon dominates regional moisture transport and precipitation (Gasse et al., 1996; Brown et al., 2003). The high arid landscapes of the study areas have a thin cover of regolith supporting only sparse grasses and small shrubs (Bhattacharyya, 1989). The region contains deeply incised valleys, typically with 1000–2000 m of local relief and peaks reaching more than 7000 m asl. Large landslides are common, and many large landslides have been identified within the region (Hewitt, 1988, 1998, 1999; Owen, 1991; Owen et al., 1995; Barnard et al., 2004; Bookhagen et al., 2005; Korup et al., 2007).

3. Methods

3.1. Field methods

Four large landslides were mapped and verified in the field using topographic maps generated from 25 m Advanced

Spaceborne Thermal Emission and Reflection Radiometer (ASTER) and 3 arc-second ($\sim$90 m) Shuttle Radar Topography Mission (SRTM) digital elevation models (DEMs) and Google Earth imagery (CGIAR-CSI, 2007; NASA, 2007).

Quartz-rich blocks on surfaces of landslide deposits were sampled for ^{10}Be surface exposure dating. About 500 g of rock was collected from the upper surface of each sampled block, to a depth of 1–5 cm. Samples were not taken in areas where landslide surfaces have been substantially modified by erosion. Six to eight blocks were sampled on each deposit to determine if any inheritance, weathering, exhumation, or toppling of blocks occurred. The location, geomorphic setting, lithology, size, shape, and weathering features of each block were recorded. Topographic shielding was determined by measuring the inclination from the block to the surrounding horizon.

3.2. Digital terrain modeling

Selected portions of the SRTM DEM were refined to better visualize landslide scarps and debris fields, to estimate slope angles, to identify large-scale rock mass discontinuities, and to extract topographic profiles. Although the 3 arc-second SRTM DEM grid is coarser than the 25 m ASTER DEM grid, the latter contained severe interpolation artifacts that made geomorphic interpretation difficult.

Areas surrounding each of the four studied landslides were extracted from the SRTM DEM and re-projected from geodetic latitude/longitude coordinates to rectilinear Universal Transverse Mercator (UTM) coordinates in order to facilitate terrain modeling. The resolution of the SRTM DEM was improved from 90 to 22.5 m raster using bilinear interpolation. Although interpolation to a smaller raster size does not add information or increase the level of detail of the DEM, it often produces smoother shaded relief images that make interpretation easier. Sets of 25 m contours were then generated for each SRTM DEM sub-area and superimposed on shaded relief images.

Landslide scarps, debris fields, and large-scale rock mass discontinuities were identified using diagnostic contour patterns, slope angle maps, and slope aspect maps supplemented by visual interpretation of satellite imagery. In particular, draping of slope angle and aspect maps over topography using three-dimensional surface visualization software with simulated illumination was an effective tool for valley-scale landform interpretation. Mapping was performed by placing a vector drawing layer on top of a series of shaded relief, contour, slope angle, and aspect layers in a geographical information system (GIS) as described by Haneberg et al. (2005) and Haneberg (2007). Topographic profiles were also extracted and used to create interpretive geomechanical cross-sections.

To make an assessment of erosion caused by the landslides, we identified catchments that contain the four large landslides reported here. The catchments were delineated on ASTER DEMs using ArcGIS 1.1 Hydro software. The surface area of each catchment upslope of the landslide deposit was determined using ArcGIS 9.1 3D Analyst. The volume of the landslide deposit was divided by the up-valley catchment area and 11.5 ka (the duration of the Holocene) to obtain a landscape-lowering rate in mm/yr. We use the Holocene to standardize landscape-lowering rates and to limit the effect of young landslides giving apparent high landscape-lowering rates.

3.3. ^{10}Be surface exposure dating

Samples from blocks were crushed and sieved to obtain the 250–500 μm size fraction. This fraction was chemically leached with a minimum of four acid leaches: aqua regia for >9 h; two 5% HF/HNO_3 leaches for $\sim$24 h; and one or more 1% HF/HNO_3 leaches each for $\sim$24 h. Acid-resistant and mafic minerals were removed from the residue after the first 5% HF/HNO_3 leach by a heavy liquid separation with lithium heteropolytungstate (density 2.7 g/cm^3). A low-background ^{9}Be carrier (^{10}Be/^{9}Be $\sim 5.7\pm2.0\times10^{-15}$ based on the weighted mean of 16 chemical blanks) was added to pure quartz, which was then dissolved in concentrated HF and fumed with perchloric acid to remove fluorine atoms. Fifteen grams of quartz was assumed for determining acid volumes used in the processing of chemical blanks. The samples were then passed through anion and cation exchange columns to remove Fe and Ti and to separate the ^{10}Be fraction. Ammonium hydroxide was added to the ^{10}Be fraction to precipitate beryllium hydroxide gel. The beryllium hydroxide was oxidized by ignition at 750 °C for 5 min in quartz crucibles. Beryllium oxide was mixed with Nb powder and loaded in steel targets for the measurement of the ^{10}Be/^{9}Be ratios by accelerator mass spectrometry at the Purdue Rare Isotope Measurement (PRIME) Laboratory at Purdue University. Six chemical blanks were measured and have a weighted mean ^{10}Be/^{9}Be ratio of $4.6\pm3.0\times10^{-15}$.

All ^{10}Be ages were calculated using the PRIME Laboratory Age Calculator (PRIME Laboratory, 2007; Table 1), which employs the scaling factors of Stone (2000) and a sea-level low-latitude production rate of 4.9±0.3 ^{10}Be atoms/g of quartz/year and a ^{10}Be half life of 1.36 Ma. No correction was made for geomagnetic field variations due to the ongoing debate regarding which correction factors are most appropriate. Please see Balco et al. (2008) for a comprehensive examination of these issues. Geomagnetic corrections to our ^{10}Be ages can change the age by up to 16%, but most ages would change by <10%. Furthermore, we have not made any corrections for erosion. However, assuming that all the blocks that were sampled weather at a moderate rate of 5 m/Ma (Small et al.'s, 1997 summit boulder erosion rate), a calculated age of 5 ka, assuming no surface erosion, would underestimate the true age by a maximum of 2%, an age of 7.5 ka by 3%, and an age of 10 ka by 4%.

We report the mean age and standard deviation of landslides, but use the weighted mean and error (M_w) to define their ages. M_w is used because the precisions of the age determinations differ. Ages calculated using both the CRONUS and PRIME Laboratory calculators are reported in Table 2 to display possible errors associated with age calculator standardization, scaling factors, and geomagnetic corrections. The samples were measured at the PRIME Laboratory, we therefore choose to use standard uncorrected ages calculated using the PRIME Laboratory Rock Age calculator. ^{10}Be ages from other studies were also recalculated with the Rock Age calculator to enable comparison with studies using different ^{10}Be age assessment techniques.

4. Landslide descriptions

4.1. Darcha landslide

The Darcha landslide deposit is located near the village of Darcha (32.667°N/77.205°E, $\sim$3350 m asl) in the Lahul Himalaya (Figs. 1 and 2). The landslide headscarp is located on the west side of the valley on a phyllite spur/ridge between $\sim$3375 and $\sim$4000 m asl and has a surface area of 0.2×10^6 m^2 (Figs. 2A and 3; Table 3). Weidinger et al. (2002) noted that the sliding plane, trending 340°/65°NE, has a stepped shape with bedding dipping into the slope perpendicular to it. The bedrock is a >2000-m-thick argillaceous flysch succession—the Phe Formation—composed of massive to laminated sandstones and siltstones alternating with finely laminated silty and carbonaceous slates (Fuchs and Linner, 1995; Weidinger et al., 2002). The Phe formation is steeply folded with southwest vergence and is intruded by diabase and gabbroic masses (Fuchs and Linner, 1995).

Table 1
Sample location, ^{10}Be terrestrial cosmogenic nuclide data, and ages from CRONUS and PRIME Laboratory calculators.

Sample name	Landform name	Latitude (°N)	Longitude (°E)	Elevation (m asl)	Thickness (cm)	Shielding correction	^{10}Be (10^5 atoms/g SiO_2)	^{10}Be ages calculated using the CRONUS calculator (ka)[a]	^{10}Be ages calculated using the PRIME Lab calculator		
									Age (ka)[b]	Age (ka)[c]	Age (ka)[d]
Darcha-1	Darcha	32.667	77.205	3375	5	0.95	3.25±0.30	8.3±1.0	8.2±0.9	8.3±0.9	7.6±0.8
Darcha-2	Darcha	32.668	77.205	3358	5	0.96	2.40±0.14	6.1±0.6	6.1±0.5	6.4±0.5	5.8±0.5
Darcha-3	Darcha	32.669	77.206	3361	2	0.97	2.74±0.12	6.7±3.0	6.7±3.0	6.9±3.1	6.3±2.8
Darcha-4	Darcha	32.669	77.205	3585	5	0.96	2.33±0.21	5.3±0.7	5.2±0.6	5.5±0.6	4.9±0.5
Darcha-5	Darcha	32.669	77.205	3371	5	0.97	2.92±0.22	7.3±0.8	7.3±0.7	7.5±0.7	6.8±0.7
Darcha-6	Darcha	32.669	77.206	3358	2	0.96	3.29±0.61	8.1±1.7	8.1±1.6	8.2±1.6	7.5±1.5
Patseo-2	Patseo	32.755	77.257	3809	5	0.97	3.81±0.23	7.5±0.8	7.4±0.6	7.6±0.6	6.7±0.6
Patseo-3	Patseo	32.755	77.257	3809	3	0.98	4.31±0.41	8.3±1.1	8.2±0.9	8.3±0.9	7.3±0.8
Patseo-4	Patseo	32.754	77.258	3795	5	0.98	4.05±0.47	8.0±1.2	8.0±1.1	8.1±1.1	7.1±0.9
Patseo-5	Patseo	32.755	77.258	3799	5	0.99	4.20±0.26	8.2±0.9	8.2±0.7	8.3±±0.7	7.3±0.6
Patseo-6[e]	Patseo	32.753	77.257	3801	5	0.98	5.76±0.13	11.4±24.8	11.3±24.7	11.2±24.6	9.9±21.5
Pang-1	Chilam	33.962	78.211	4214	3	0.98	5.74±0.19	8.8±0.8	8.6±0.6	8.7±0.6	7.3±0.5
Pang-3	Chilam	33.962	78.211	4213	5	0.98	5.51±0.26	8.6±0.9	8.4±0.7	8.5±0.7	7.2±0.6
Pang-4	Chilam	33.962	78.211	4215	3	0.98	5.22±0.21	8.0±0.8	7.8±0.6	8.0±0.6	6.7±0.5
Pang-5	Chilam	33.962	78.211	4217	5	0.98	5.83±0.32	9.1±0.9	8.9±0.7	8.9±0.7	7.5±0.6
Pang-6	Chilam	33.962	78.211	4216	5	0.98	5.79±0.20	9.0±0.8	8.8±0.6	8.9±0.6	7.5±0.5
Pang-7	Chilam	33.962	78.212	4212	4	0.98	5.56±0.17	8.6±0.8	8.4±0.6	8.5±0.6	7.2±0.5
COS1	Kelang Serai	32.816	77.441	5000	2[f]	0.99	5.87±0.23	6.2±0.6	6.1±0.4	6.4±0.5	5.1±0.4
COS2	Kelang Serai	32.816	77.448	4717	2[f]	0.99	5.12±0.23	6.2±0.6	6.1±0.5	6.4±0.5	5.2±0.4
COS3	Kelang Serai	32.822	77.459	4780	2[f]	0.99	5.24±0.23	6.1±0.6	6.1±0.5	6.3±0.5	5.2±0.4
India-2	Kelang Serai	32.820	77.455	4621	2	1.00	5.13±0.25	6.4±0.6	6.3±0.5	6.6±0.5	5.5±0.4
India-3	Kelang Serai	32.821	77.455	4621	3	1.00	5.11±0.32	6.4±0.5	6.4±0.6	6.6±0.6	5.5±0.5
India-4	Kelang Serai	32.821	77.455	4625	3	1.00	4.90±0.19	6.2±0.6	6.1±0.4	6.3±0.5	5.3±0.4
India-5	Kelang Serai	32.820	77.454	4638	4	0.98	5.38±0.25	6.9±0.7	6.8±0.5	7.0±0.5	5.8±0.5
India-6	Kelang Serai	32.820	77.454	4635	2	0.98	5.71±0.29	7.2±0.7	7.1±0.6	7.3±0.6	6.1±0.5
India-7	Kelang Serai	32.820	77.454	4634	4	1.00	5.69±0.32	7.2±0.7	7.1±0.6	7.3±0.6	6.1±0.5
India-8	Kelang Serai	32.818	77.451	4682	4	1.00	5.24±0.20	6.5±0.6	6.4±0.5	6.6±0.5	5.5±0.4
India-9	Kelang Serai	32.820	77.447	4650	2	0.98	5.43±0.24	6.8±0.7	6.8±0.5	7.0±0.5	5.8±0.4
TCB-1	Tianchi	43.902	88.122	1923	2[f]	0.98	2.52±0.25	11.6±1.5	11.3±1.3	11.7±1.4	11.3±1.3
TCB-2	Tianchi	43.901	88.121	1944	2[f]	0.98	4.10±0.14	18.5±1.7	18.2±1.2	18.5±1.3	17.9±1.3
TCB-3	Tianchi	43.900	88.121	1938	2[f]	0.98	3.02±0.40	13.7±2.2	13.4±2.0	13.8±20.	13.3±2.0
TCB-6	Tianchi	43.897	88.118	1944	2[f]	0.98	2.53±0.14	11.4±1.2	11.2±0.9	11.5±1.0	11.1±0.9
TCB-7	Tianchi	43.898	88.119	1922	2[f]	0.98	1.66±0.15	7.6±1.0	7.5±0.8	7.8±0.9	7.5±0.8
G1	Rangatoli	30.389	79.334	1330	2[f]	1.00	3.72±0.04	3.4±0.4	3.5±0.4	3.7±0.4	4.0±0.4
G2	Rangatoli	30.389	79.334	1335	2[f]	0.99	3.05±0.03	2.7±0.3	2.8±0.3	3.1±.3	3.3±0.4
G3	Rangatoli	30.389	79.333	1340	2[f]	0.99	7.97±0.06	7.2±0.8	7.4±0.7	7.6±0.7	8.1±0.8
G4	Dear	30.422	79.347	1490	2[f]	1.00	1.22±0.04	9.9±0.9	10.2±0.7	10.2±0.7	10.7±0.7
G5	Dear	30.422	79.347	1490	2[f]	0.99	1.30±0.05	10.6±1.0	10.9±0.8	10.8±0.8	11.4±0.8
G6	Dear	30.422	79.348	1485	2[f]	1.00	1.23±0.04	10.0±0.9	10.3±0.7	10.3±0.7	10.8±0.8
G7	Dear	30.429	79.348	1530	2[f]	0.99	1.21±0.05	9.6±0.9	9.8±0.7	9.8±0.7	10.3±0.7
G8	Dear	30.429	79.349	1530	2[f]	0.99	1.20±0.05	9.5±0.9	9.7±0.7	9.8±0.7	10.3±0.8
NDL 24	Milan	30.430	80.160	3446	2[f]	0.97	1.90±0.65	4.8±1.7	4.7±1.6	5.0±1.7	4.6±1.6
NDL 25	Milan	30.430	80.160	3335	2[f]	0.97	3.14±0.14	8.4±0.8	8.3±0.6	8.4±0.6	7.8±0.6
NDL 26	Milan	30.430	80.160	3416	2[f]	0.97	2.82±0.16	7.2±0.7	7.1±0.6	7.3±0.6	6.7±0.6
NDL 27	Milan	30.430	80.160	3435	2[f]	0.97	3.23±0.80	8.2±0.7	8.1±0.5	8.2±05	7.5±0.5
E99	Yaral	27.850	86.800	4114	2[f]	0.98	4.34±0.11	8.1±0.7	8.0±0.5	8.2±0.5	7.3±0.5
E100	Yaral	27.850	86.800	4058	2[f]	0.98	4.14±0.11	7.9±0.7	7.8±0.5	8.1±0.5	7.2±0.5
E101	Yaral	27.850	86.800	4058	2[f]	0.98	4.23±0.13	8.1±0.7	8.0±0.5	8.2±0.6	7.3±0.5
E109	Pangbache	27.860	86.790	3985	2[f]	0.98	4.96±0.23	9.9±1.0	9.7±0.7	9.9±0.8	8.8±0.7
E110	Pangbache	27.850	86.790	3970	2[f]	0.98	11.2±0.34	22.5±2.1	22.1±1.5	20.9±1.4	18.6±1.3
E111	Pangbache	27.850	86.790	3979	2[f]	0.98	4.29±0.13	8.6±0.8	8.4±0.6	8.6±0.6	7.7±0.5
KTM10	Tsergo Ri	28.209	85.608	4831	2[f]	0.99	33.7±0.83	44.6±4.1	43.4±2.9	37.1±2.5	31.1±2.1
KTM11	Tsergo Ri	28.209	85.608	4843	2[f]	0.99	18.0±0.37	23.6±2.1	22.9±1.5	21.5±1.4	18.0±1.2
KTM12	Tsergo Ri	28.209	85.608	4848	2[f]	0.99	28.5±0.44	37.4±3.3	36.3±2.3	32.1±2.1	26.8±1.7
K2-36	Gomboro	35.729	75.663	2828	2[f]	0.94	4.65±0.13	15.0±1.4	14.8±1.0	14.5±1.0	13.5±0.9
K2-37	Gomboro	35.729	75.663	2833	2[f]	0.95	4.76±0.13	15.2±1.4	14.9±1.0	14.6±1.0	13.6±0.9
K2-38	Gomboro	35.730	75.663	2832	2[f]	0.95	4.82±0.15	15.4±1.4	15.1±1.0	14.8±1.0	13.8±1.0
K2-39	Gomboro	35.730	75.662	2837	2[f]	0.95	4.60±0.13	14.6±1.3	14.4±1.0	14.1±0.9	13.1±0.9
K2-40	Gomboro	35.730	75.662	2835	2[f]	0.95	4.61±0.13	14.7±1.3	14.4±1.0	14.2±0.9	13.1±0.9
K2-41	Gomboro	35.729	75.663	2839	2[f]	0.95	4.04±0.16	12.8±1.2	12.6±0.9	12.5±0.9	11.5±0.8
Ron68	Rongbuk	28.2023	86.8235	5028	1.5	0.99	7.12±0.21	8.6±0.8	8.3±0.6	8.6±0.6	7.1±0.5
Ron69	Rongbuk	28.2024	86.8236	5013	1.0	0.99	7.29±0.19	8.8±0.8	8.5±0.6	8.8±0.6	7.3±0.5
Ron70	Rongbuk	28.2024	86.8235	5009	3.0	0.99	6.67±0.17	8.1±0.7	7.9±0.5	8.2±0.5	6.9±0.5
Ron71	Rongbuk	28.2019	86.8235	5015	2.5	0.97	7.00±0.14	8.6±0.8	8.4±0.5	8.6±0.5	7.2±0.5
Ron72	Rongbuk	28.2018	86.8243	5031	4.0	0.98	6.93±0.17	8.4±0.8	8.3±0.5	8.5±0.6	7.1±0.5
Ron73A	Rongbuk	28.2015	86.8246	5019	3.0	0.98	6.74±0.18	8.2±0.7	8.0±0.5	8.3±0.5	6.9±0.5
Ron73B	Rongbuk	28.2015	86.8246	5019	3.0	0.98	7.00±0.18	8.5±0.8	8.3±0.6	8.6±0.6	7.1±0.5

Notes: Assumes zero erosion rate, standard pressure, and ρ=2.7 g/cm^3 for all samples.
[a] CRONUS ages calculated using Lal (1991)/Stone (2000) scaling scheme.
[b] Age calculated using scaling model of Stone (2000).
[c] Age calculated using scaling model of Nishiizumi et al. (1989).
[d] Age calculated using scaling model of Desilets and Zreda (2003).
[e] The large error of sample Patseo-6 is due to the small ^{10}Be volume and large counting errors.
[f] A 2 cm sample thickness was assumed in recalculating the age.

Table 2
Characteristics of rock avalanches with numerical ages. M_w is the weighted mean age and error.

Landslide	Latitude	Longitude	Type	M_w age (ka)	MSWD[a]	Age $\mu\pm\sigma$ (ka)[b]	Volume ($\times10^6$ m^3)	Author
Bualtar 1	36.2	74.76	Historical	1986 A.D.	N/A	N/A	20	Hewitt (1988)
Bualtar 2	36.2	74.76	Historical	1986 A.D.	N/A	N/A	7	Hewitt (1988)
Bualtar 3	36.2	74.76	Historical	1986 A.D.	N/A	N/A	3	Hewitt (1988)
Hattian Bala	34.16	73.74	Historical	2005 A.D.	N/A	N/A	85	Dunning et al. (2007)
Kaza	32.18	78.09	^{14}C	3.0±0.1	N/A	N/A	500	Bookhagen et al. (2005)
Rangatoli	30.39	79.33	^{10}Be	N/A	N/A	3.1±0.4	N/A	Barnard et al. (2001)
Kelang Serai	32.82	77.44	^{10}Be	6.6±0.4	0.49	6.6±0.4	520	This study
Kelang Serai	32.82	77.44	^{10}Be	6.1±0.5	0.01	6.1±0.04	900	Mitchell et al. (2007)
Darcha	32.67	77.2	^{10}Be	7.7±1.0	0.21	7.6±0.7	10	This study
Patseo	32.76	77.26	^{10}Be	7.9±0.8	0.16	8.6±1.5	128	This study
Ghoro Choh	35.64	75.5	^{14}C	<7.95[c]	N/A	N/A	60	Hewitt (1999)
Rongbuk	28.2	86.82	^{10}Be	8.2±0.4	0.12	8.3±0.2	~2	Owen et al., in prep
Chilam	33.96	78.21	^{10}Be	8.5±0.5	0.32	8.5±0.4	240	This study
Kuppa	31.43	78.24	^{14}C	6.1±0.07–8.4±.0.02[c]	N/A	N/A	600	Bookhagen et al. (2005)
Sichling	32.11	78.18	^{14}C	7.6±0.1–9.7±0.1[c]	N/A	N/A	1,400	Bookhagen et al. (2005)
Dear	30.42	79.35	^{10}Be	10.2±0.6	0.32	10.2±0.5	N/A	Barnard et al. (2001)
Tianchi	43.9	88.12	^{10}Be	12.0±1.5	0.36	12.5±0.5	N/A	Yi et al. (2006)
Gomboro	35.73	75.66	^{10}Be	14.3±0.8	0.76	14.4±0.9	N/A	Seong et al. (2008)
Shaso	31.72	78.51	^{14}C	<31.8±0.5[c]	N/A	N/A	600	Bookhagen et al. (2005)
Chango	32.07	78.59	^{14}C	<33.1±0.3[c]	0.04	N/A	1000	Bookhagen et al. (2005)
Tsergo Ri	28.21	85.61	^{10}Be	N/A	N/A	34.2±10.4	~10,000	Barnard et al. (2006)
Tsergo Ri[d]	28.21	85.61	Fission track	N/A	N/A	~100,000*	~10,000	Wagner (1995)

[a] The mean square of weighted deviates (MSWD) is a statistical indicator that represents the likelihood of one age population.
[b] The mean age with standard deviation of ages for error is represented by $\mu\pm\sigma$.
[c] Calibrated using CalPal[1].
[d] Not recalculated.

The landslide deposit, which consists almost entirely of phyllite blocks, has been described by Fuchs and Linner (1995), Owen et al. (1995), and Weidinger et al. (2002). The deposit has a crescent-shaped toe on the Bhaga River floodplain (Fig. 2C). The toe has an area of ~0.4×10^6 m^2 and contains a parabolic-shaped depression located in the center of the deposit. The toe of the landslide appears to have displaced the confluence of the Bhaga River and its tributary to the northwest, confining the flow to a braid plain between the toe and the adjacent rising slope.

The toe is marked by numerous subparallel, parabolic, and longitudinal ridges that are separated by shear zones that are generally parallel to the edge of the deposit (Fig. 2B and D). They may represent secondary sliding zones parallel to the basal surface and tertiary zones that are vertical (Schramm et al., 1998). Schramm et al. (1998) suggest that these sliding zones develop to accommodate the non-uniform movement of the landslide mass and to allow internal deformation. Similar sliding zones have been described in other large, long run-out landslides such as the

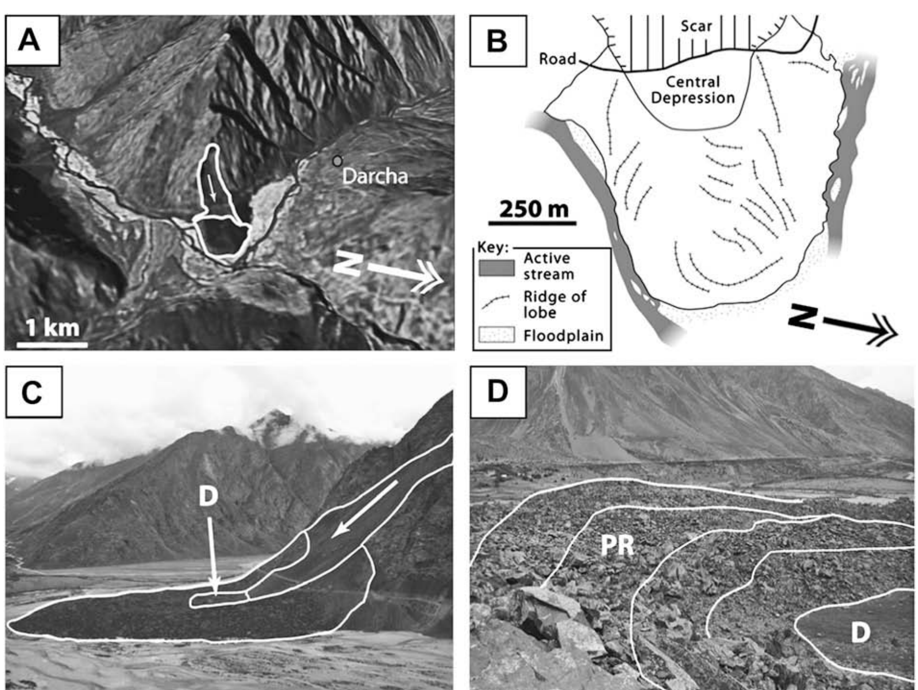

Fig. 2. The Darcha landslide in the Lahul Himalaya. (A) Google Earth image of the landslide and geomorphic setting. (B) Simplified geomorphic map of the landslide, adapted from Owen et al. (1995). (C) South and (D) southeast views of the landslide showing its ridged and lobate form. The oblique white arrow highlights the landslide scar and the direction of landslide advance (D, depression, PR, parabolic ridges). The highway that traverses the landslide scar in (C) provides a scale.

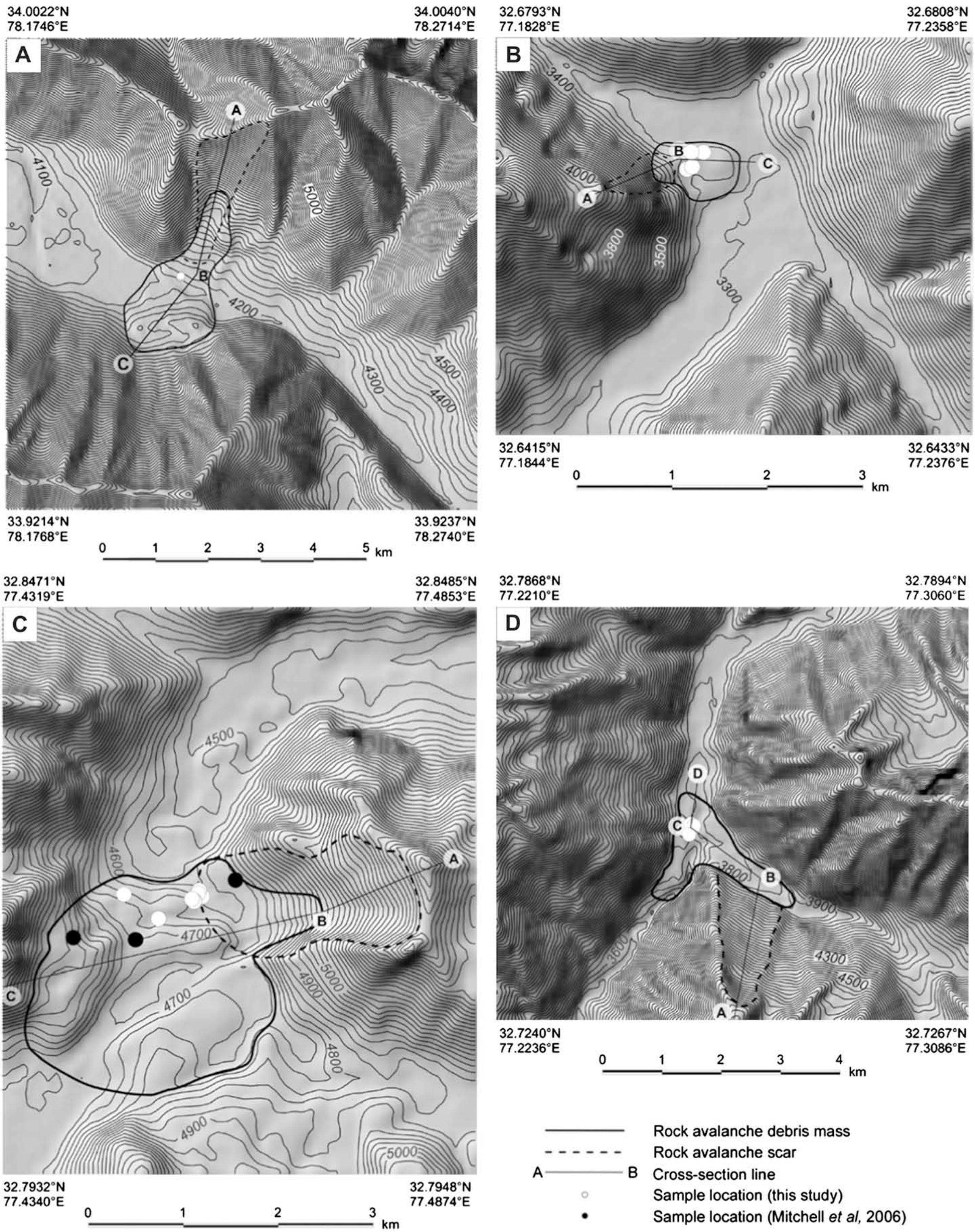

Fig. 3. DEM with contours showing the topography, deposit, scar, and sample locations (white dots) for ^{10}Be dating for the (A) Chilam, (B) Darcha, (C) Kelang Serai, and (D) Patseo landslides. Lines in A, B, C, and D show the locations of the longitudinal profiles shown in Fig. 12. The black dots in (C) are sample locations of Mitchell et al. (2007).

Table 3
Details of rock avalanche geometric aspects; including surface area, volume, emplacement velocity, and slope controls.

Landslide	Scar area (m^2)	Debris area (m^2)	Calculated thickness[a] (m)	Estimated thickness[b] (m)	Thickness ratio[c]	Debris volume (m^3)	V_{max} (m/s)	Slope of slip surface (°)	Fahr-böschung (°)	Energy slope (°)
Darcha	200,000	400,000	6	25	4	10,000,000	61	50	24	30
Patseo	1,600,000	1,700,000	12	75	6	127,500,000	78	28	15	16
Kelang Serai	2,200,000	5,200,000	21	100	5	520,000,000	77	28	9	12
Chilam	1,800,000	3,200,000	16	75	5	240,000,000	67	38	13	18

[a] Back-calculated using Iverson (2006) area–volume relationship constrained by measured area.
[b] Estimated from contour maps developed for this project.
[c] Estimated/calculated thickness.

Keylong Serai and the Tsergo Ri (Schramm et al., 1998; Mitchell et al., 2007).

The surface of the deposit is dominated by large, very angular blocks >1 m in diameter. Some blocks exceed 10 m in length and have jigsaw morphology, with numerous centimeter-size fractures separating the block into several pieces that still fit together (Fig. 4A). Blocks on the toe of the deposit form an open framework with some sand and fine gravel—the result of bedrock shattering during transport and emplacement. Block surfaces have a dark brown to black varnish and intergrown greenish-gray lichen up to ~30 cm in diameter and *Rhicocarpum geographicum* in irregular masses 10–15 cm in length. These lichen are not suitable for dating due to their highly irregular shapes, communal growth, and the occurrence of new growth over old dead lichens. Moreover, they reach their maximum diameter within a few hundred years. Loose flakes are present on some blocks, indicating that exfoliation is active on rock surfaces. Exfoliation block surfaces are also varnished, suggesting that varnish formation is rapid. Six blocks (Darcha 1–6) were sampled for ^{10}Be surface exposure dating (Fig. 5A).

4.2. Patseo landslide

The Patseo landslide deposit traverses the Bhaga Valley (32.755°N/77.257°E, ~3800 m asl; Figs. 1 and 6A). The landslide deposit was first described by Fuchs and Linner (1995) as a rock avalanche. Subsequently it was described by Owen et al. (1997), Weidinger et al. (2002), and Fort (2003). The headscarp (Fig. 3), located on a northeast-facing slope between ~3900 and ~4925 m asl, has an area of 1.6×10^6 m^2 and is parallel or subparallel to a major lithologic structure in the bedrock (Weidinger et al., 2002; Table 3). This structure is north dipping bedding planes related to the Patseo syncline, a Paleozoic succession consisting of the Thaple Formation, Muth quartzites, and the Lipak Formation (Fuchs and Linner, 1995; Weidinger et al., 2002). Weidinger and Nuschej (2001) suggest the headscarp is located west of the landslide deposit while Mitchell et al. (2001) suggest it is located to the east. We prefer the eastern location on the northeast-facing slope based on field observation of the planar scarp. However, we acknowledge that large fans deposits make it difficult to determine the former sliding planes and that both scarp locations could have contributed to the deposit (Weidinger et al., 2002). Choice of scarp, however, does not affect the deposit volume, which is calculated from valley fill.

The Patseo landslide deposit has an area of 1.7×10^6 m^2 with a hummocky surface that extends northeast and up valley from the headscarp. The deposit fills the valley and has created a knickpoint on the Bhaga River. The Bhaga River has infilled upstream of the deposit. Although no lake sediments are present at the surface behind the landslide deposit, lake formation was likely after the deposit was emplaced. The deposit was overtopped and incised,

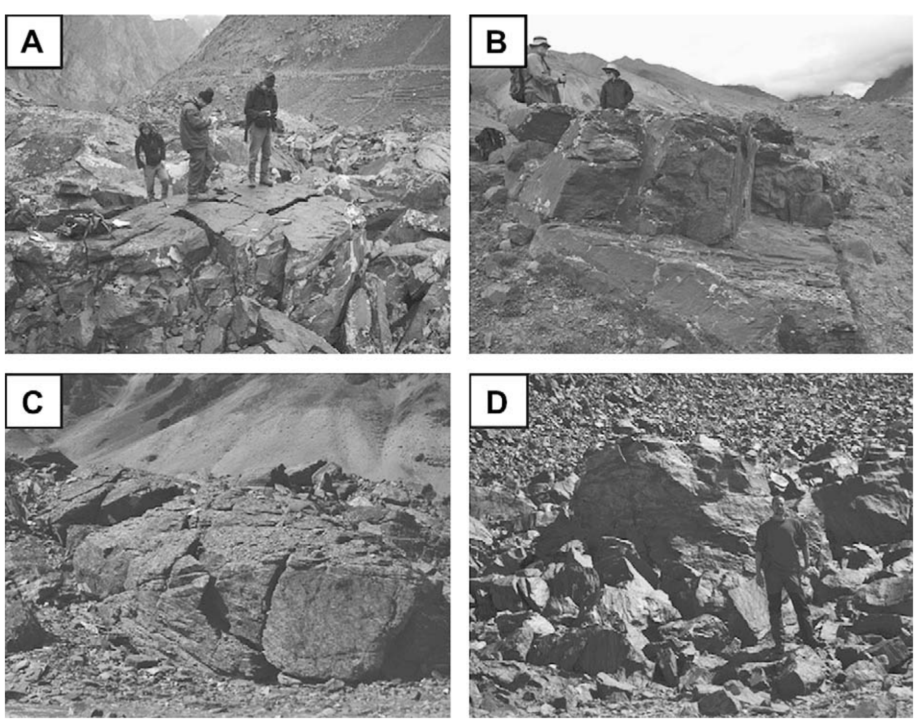

Fig. 4. Views of “jigsaw blocks” on the (A) Darcha, (B) Patseo, (C) Kelang Serai, and (D) Chilam landslides. The block in (C) is ~10 m in diameter.

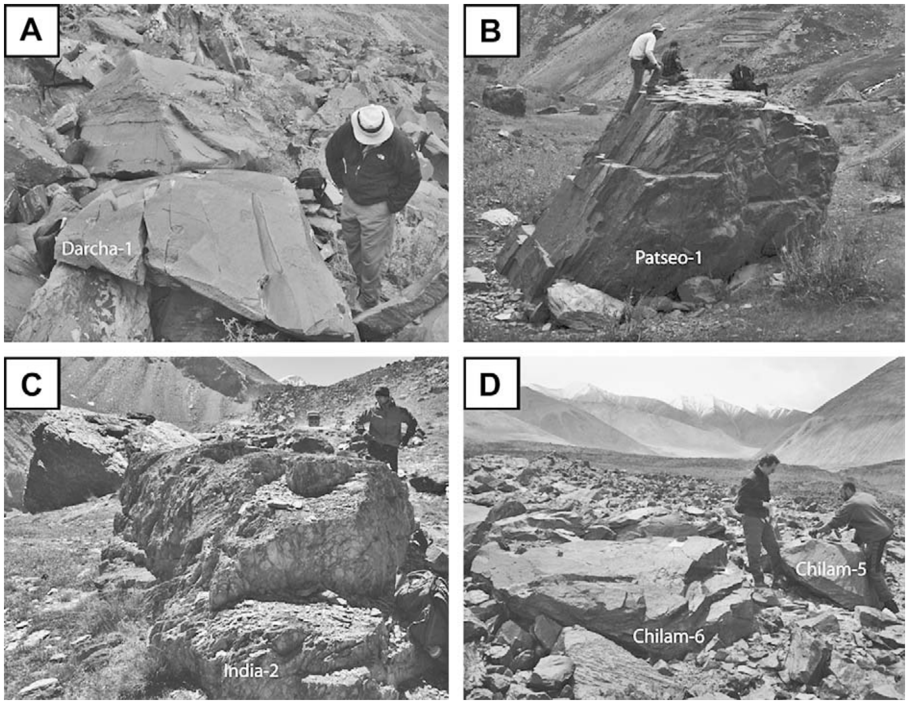

Fig. 5. Typical blocks sampled for ^{10}Be surface exposure dating on the (A) Darcha, (B) Patseo, (C) Kelang Serai, and (D) Chilam landslides. Sample numbers are shown on the blocks.

creating a narrow steep-sided channel that is 25–50 m deep. South of the deposit the river enters a narrow gorge. The river does not cut down below the base of the avalanche debris, therefore, the depth of the channel provides a minimum thickness for the deposit (>50 m). This thickness can be used to verify the DEM-based modeled thickness of the deposit (Table 3). Color banding is evident in the landslide deposit and can be seen in the banks of the incised channel (Fig. 6D). A small lake is trapped between the deposit and the cross-valley hillslope to the northwest edge of the deposit (Fig. 6C).

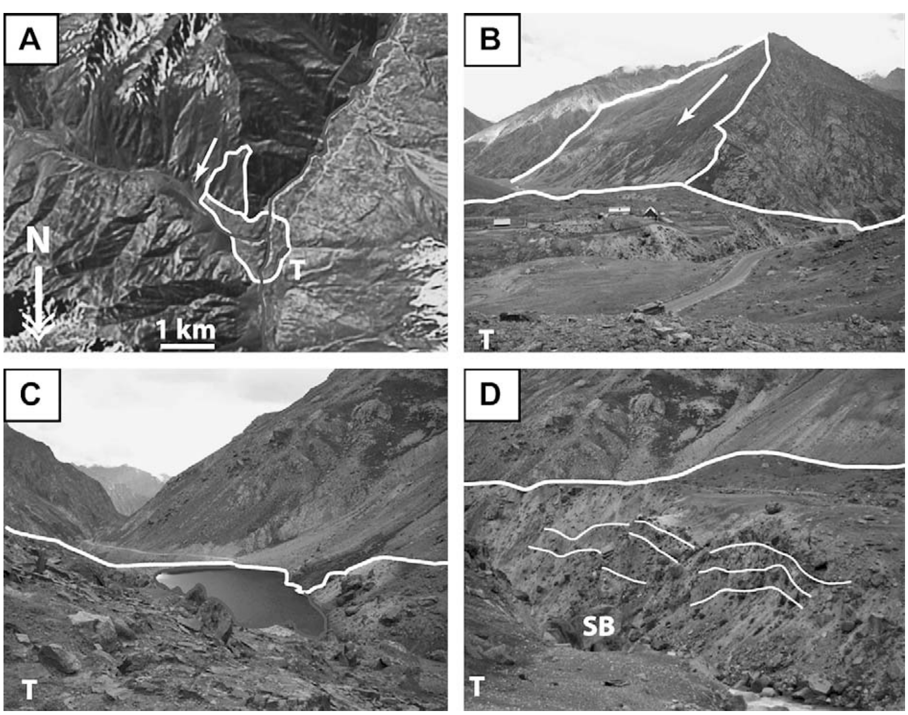

Fig. 6. The Patseo landslide in the Lahul Himalaya. (A) Google Earth image showing the location and geomorphic setting of the landslide. (B) Southeast view of landslide failure slope (oblique white arrow) and landslide debris in the foreground and middle ground. The buildings and truck provide scale. (C) View south from the highest ridge at the top of the landslide toe (T) showing the landslide debris choking the valley and a small lake within the landslide hummocks. The highway in the middle ground provides a scale. (D) West view of stream exposure within the landslide debris showing shattered bedrock blocks. Labeled shattered bedrock (SB) block is about 3 m in diameter. The bedrock stratigraphy is preserved within the landslide debris and is highlighted by thin white lines.

The surface of the deposit comprises phyllite, psammite, and carbonate debris from the Karsha and Phe Formations that ranges from sand to cobble size with many very angular blocks 1 to >5 m in diameter (Weidinger et al., 2002). The blocks have a medium to dark varnish, inter grown greenish-gray lichen up to ~30 cm in diameter, possible *Rhicocarpum geographicum* in irregular masses 2–3 cm in length, and are located on the crests and slopes of hummocks. Lichen have the same morphology as at the Darcha site and would have reached their maximum diameter in a few hundred years. Areas on block surfaces where rock chips have spalled are typically light tan in color, suggesting that varnish does not accumulate as rapidly as the Darcha site. Some blocks have multi-directional striations on their surfaces and many are broken into jigsaw blocks (Fig. 4B). Large extremely shattered blocks are also exposed in the sides of the channel that cuts through the deposit. Angular rubble is present around some blocks, likely due to active freeze-thaw activity. Grass and brush cover most of the deposit. Some of the deposit has been terraced for farming and building construction (Fig. 6B). Six blocks were sampled for ^{10}Be surface exposure dating (Patseo 1–6; Fig. 5B).

4.3. Kelang Serai landslide

The Kelang Serai (or Sarai Kenlung) landslide deposit is located in the Yunan Valley (32.820°N/77.454°E ~4650 m asl; Figs. 1 and 7A). Fuchs et al. (1995), Weidinger et al. (2002), Fort (2003), and Mitchell and Linner (2007) have described this landslide. Based on unreported ^{14}C ages from associated lacustrine sediments obtained by P. Taylor, Fort (2003) suggested that this landslide formed during the Holocene. Mitchell et al. (2007), who included estimates of its size and a detailed geomorphic map (Fig. 7B), estimated that the landslide advanced at a speed of up to 80 m/s and reported three ^{10}Be ages that had a weighted mean of 7.5±0.1 ka.

Three distinct scars are present on the northwest-trending ridge on the east side of the valley at this site (Fig. 7A). Landslide deposits are associated with each scar. We investigated in detail the largest scar and landslide deposit in our study. The deposits associated with the other two scarps have similar weathering characteristics, suggesting that all three lobes formed at the same time. However, it is possible that the lobes formed successively during a short period of geologic time.

The large planar scarp associated with the landslide we studied extends from ~4700 to ~5425 m asl has an area of 2.2×10^{6} m^2 and is bounded to the south by a nearly vertical ridge (Fig. 7C; Table 3). The bedrock is composed of the Thaple conglomerates, Muth Quartzites, and Lipak Formation, which dominantly consist of conglomerate, quartzite, sandstone, slate, and dolomite (Fuchs and Linner, 1995; Weidinger et al., 2002). Their bedding planes, which likely controlled the formation of the sliding surface, are deformed into a large northeast-trending recumbent fold (Weidinger et al., 2002).

This landslide deposit covers part of the Yünan Chu River floodplain and has a surface area of 5.2×10^{6} m^2. The surface of the landslide is hummocky, consisting of angular, cobble- to pebble-sized clasts derived from shattered bedrock. Large (>1 m) shattered angular blocks are also present and have a dark varnish on stable surfaces. Surfaces of landslide blocks that have been exfoliated or weathered are tan in color. Eight blocks (India 2–9) were sampled for ^{10}Be surface exposure dating (Fig. 5C), supplementing ages reported by Mitchell et al. (2007).

Mitchell et al. (2007) noted the presence of jigsaw blocks and distinctive color banding in the landslide deposit that mimics the stratigraphy of source rocks in the scarp (Fig. 4C). On the basis of Hewitt's (2002) classification, they assigned this landslide to a Type IV rock avalanche, which are associated with extreme impact on cross-valley slopes. This assignment is supported by our observation that the deposit extends up to an elevation of ~4900 m asl on the cross-valley hillside, indicating that the main deposit traveled across the valley and ~200 m up the opposing hillside before falling back to the southwest.

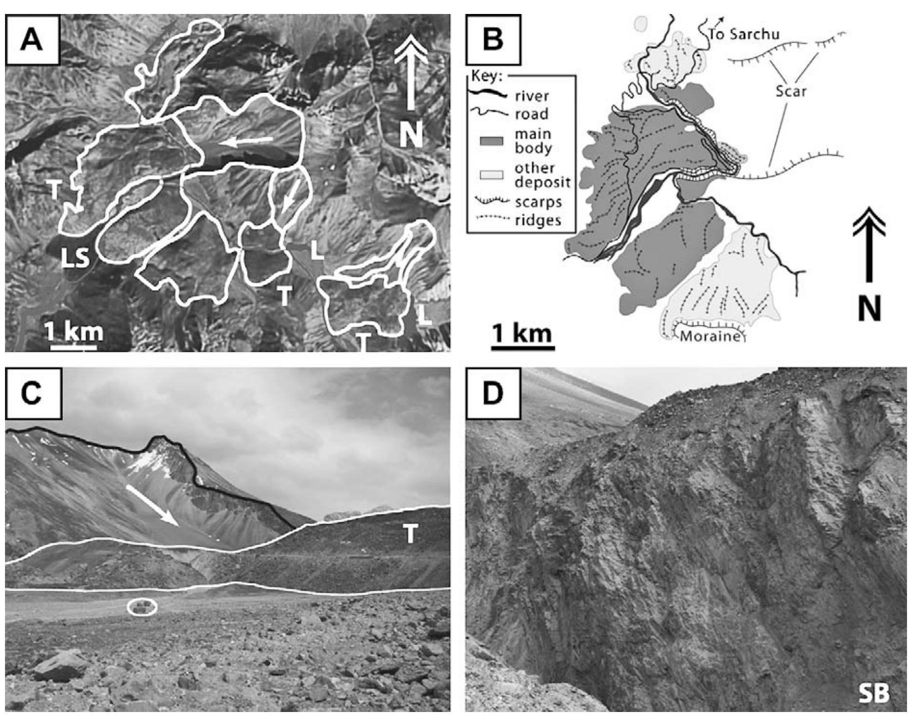

Fig. 7. The Kelang Serai landslide in the Lahul Himalaya. (A) Google Earth image of the landslide showing its location and setting. The white arrows highlight the location of the landslide scars and direction of advance of landslide debris (LS, lake sediments, L, contemporary lake, and T, landslide toe). (B) Simplified geomorphic map modified from Mitchell et al. (2007). (C) South view of the headscarp of the main failure (oblique white arrow) and the edge of the landslide debris (T). Four trucks enclosed by the white oval provide scale. (D) South view of shattered bedrock (SB) incorporated into the landslide debris. The field of view is about 20 m.

The three landslides at this location dammed the Yünan Chu River and its tributary river, resulting in the formation of three paleo-lakes (Fig. 7A). The largest of the three lakes formed on the main Yünan Chu River trunk. Approximately 20–30 m of lacustrine sediment was deposited in this lake. The sediments comprise 1-mm- to 1-cm-thick rhythmite beds composed of ~95% clay and ~5% silt with rare small pebbles and desiccation cracks along some horizons. Weidinger et al. (2002) estimated that it took 2500–3500 years for these deposits to form based on sedimentation rates. The drainage of this large paleo-lake likely cut the narrow steep-sided channel that crosses the toe the largest landslide deposit. The walls of the channel reveal landslide blocks >1 m in diameter that are supported by a matrix of shattered rock (Fig. 7D). The other two lakes were not investigated in the field due to difficulties of access. Google Earth imagery, however, shows that they still contain water.

4.4. *Chilam landslide*

The Chilam landslide deposit is located in the Loi Yogma Valley (33.962°N/78.211°E, ~4200 m asl) (Figs. 1 and 8). The head scarp, which has an area of 1.8×10^6 m^2 (Fig. 8A; Table 3), is located on the north side of the valley on a south facing ridge and extends from ~4250 to ~5600 m asl (Fig. 3). The rock-slope is composed of Ladakh Batholith and Khardung Volcanics (Dunlap et al., 1998). Dunlap et al. (1998) show they have been deformed by shear along the Karakoram Fault at greenschist facies as recently as 13 Ma. They also show that the Ladakh Batholith is heavily fractured and the Khardung Volcanics exhibit northeast dipping tectonic cleavage. Levees flank the landslide deposit and extend from the base of the scarp below ~4600 m asl and to the toe at 4200 m asl (Fig. 8B). The levees consist of clast-supported pebble- to cobble-sized rock clasts with a sand matrix.

The landslide deposit is hummocky and has an area of 3.2×10^6 m^2. Its surface is covered by angular pebble- to cobble-sized diorite and volcanic clasts and blocks up to 1 m in diameter (Fig. 8D). The deposit extends across the valley and part way up the opposing hillslope to the south, where it is marked by numerous crescent-shaped ridges. Other ridges on the surface of the deposit are aligned parallel to flow direction (Fig. 4C and D) where there are clast-supported, open framework, jigsaw blocks >5 m in diameter. The ridges are coarser than the levees or the surfaces (0.5–1.0 m) between them. The large blocks in the ridges are deeply varnished, whereas blocks between the ridges are lighter in color. Block surfaces are tan in color where weathering is significant. In some places, weathering pits reach 3 cm deep. Six blocks were sampled for ^{10}Be surface exposure dating (Pang-1, 3–7; Fig. 5D).

The Loi Yogma River has incised the deposit forming a narrow channel bordered by small terraces. Color-banded layers of cobble- and pebble-size clasts of shattered landslide-transported bedrock are exposed in the channel walls (Fig. 8C). The shattered bedrock clasts are supported by a sandy pebbly matrix. Large intact blocks and jigsaw blocks are also present within the deposit. The landslide likely dammed the Loi Yogma River, but as of yet no evidence for a paleo-lake has been found.

5. Ages of landslides

The ^{10}Be ages for each of the four landslides we studied are presented in Fig. 9 and Table 1. ^{10}Be ages for these four landslides and recalculated published ^{10}Be ages of other landslides in the Himalaya (Table 2) were analyzed using the mean square of weighted deviates (MSWD) method of McDougall and Harrison (1999) to assess whether they statistically represent a single population or event. Outliers were removed iteratively from the data set (Fig. 9). This process was repeated until the MSWD was <1. Using this approach, Darcha 2 and 4, TCB 2 and 7, NDL 24, G3, and E100 were eliminated from the data set and are not considered

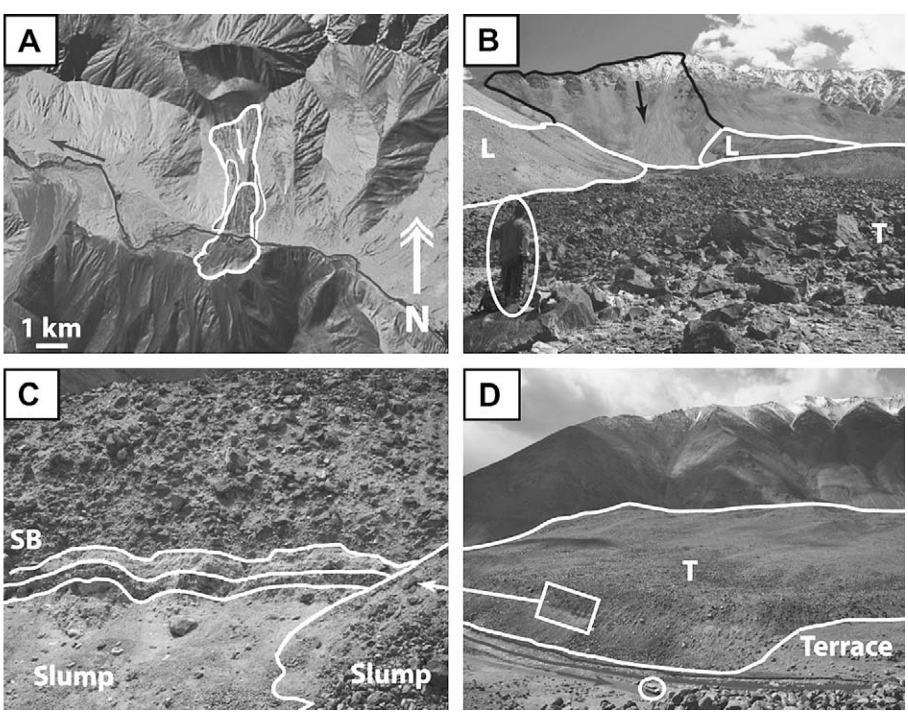

Fig. 8. The Chilam landslide in the Ladakh Himalaya. (A) Google Earth image of the landslide showing its location and setting. The white arrow highlights the landslide scar and the direction of landslide advance. (B) View northeast showing the landslide scar (black arrow) and the landslide debris. Levees created by advancing debris are indicated by L. The circle encloses a person for scale. (C) South view of the internal structure of the landslide debris. The white lines highlight preserved, highly shattered bedrock debris (SB). (D) South view across the landslide debris showing the toe (T) of the landslide. The circle encloses a jeep for scale, and the box highlights the section shown in part C.

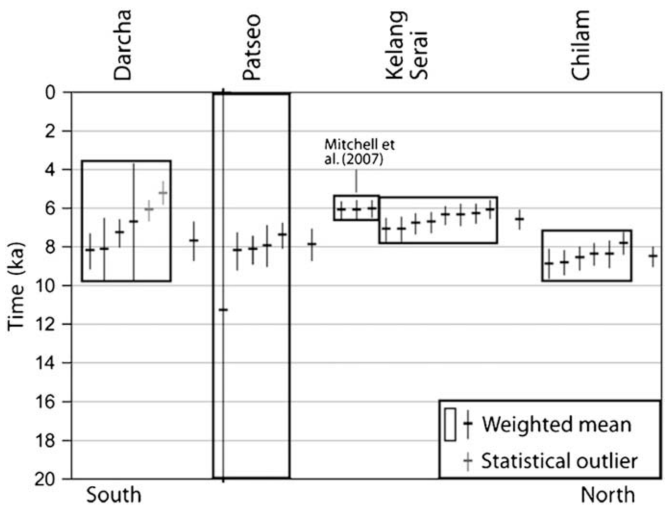

Fig. 9. [10]Be and weighted mean ages for landslides examined in this study. Statistical outliers were not used in weighted mean age calculations. Weighted mean ages are plotted to the right of the data block for each landslide. [10]Be ages from Mitchell et al. (2007) were recalculated using the PRIME Laboratory calculator (see text for details).

further in our analysis. Statistical analysis was not possible for the Rangatoli and Tsergo Ri landslides and the Pangbache terrace because only two ^{10}Be ages remain for each after the MSWD analysis. For these surfaces we report the mean age and the standard deviation (Table 2).

With Darcha 2 and 4 sample ages removed, the mean and standard deviation of the remaining four ^{10}Be ages on the Darcha landslide is 7.6±0.7 ka (Table 2). The M_w age and error is 7.7±1.0 ka, and MSWD is 0.21 (Fig. 9). The mean and standard deviation and M_w ^{10}Be ages of the Patseo landslide are 8.6±1.5 and 7.9±0.8 ka, respectively, with a MSWD of 0.16 for the latter. Retaining or removing sample Patseo-6 does not affect either ^{10}Be age due to its large error. The mean and standard deviation ^{10}Be age of the Kelang Serai landslide is 6.6±0.4 ka; its M_w is 6.6±0.4 ka and MSWD is 0.49. These ages overlap the M_w ^{10}Be age on this landslide reported by Mitchell et al. (2007), which we have recalculated using the scaling methods adopted in our study as 6.1±0.5 ka and MSWD of 0.01. The recalculated age differs from those reported by Mitchell et al. (2007) because they have not been corrected for geomagnetic variability. The mean and standard deviation and M_w ^{10}Be ages of the Chilam landslide are 8.5±0.4 and 8.5±0.5 ka (MSWD of 0.32), respectively. The MSWD for all landslides is low, suggesting that each set of calculated ages represents one population. The M_w ages of the Darcha, Patseo, and Chilam landslides are within 1 standard deviation of one another. Therefore, it is possible, but not proven, that they occurred simultaneously.

6. Comparative geometry and geomechanics

Relevant geometric aspects of the four landslides are summarized in Table 3. Planimetric areas were estimated from the debris masses and scarp outlines in Fig. 3, Debris volumes were calculated as the product of the debris planimetric areas and typical thickness values visually estimated from the DEM contours. The thickness estimates are subjective and do not account for any topography buried beneath the landslide debris, therefore, their accuracy is probably no better than ±25%.

The energy slope was calculated by visually inferring the centers of mass for the pre-slide rock and post-slide debris masses. The energy slope is different from the *Fahrböschung* of Heim (1932), which is the angle of a line from the top of the landslide headscarp to the most distal part of the deposit rather than a line connecting the two centers of mass. Maximum debris velocity was calculated assuming dry frictional material and using the following relationship:

$$z_{\max} = v_{\max}^2/2g \quad (1)$$

where $z_{\max}$ is the maximum vertical distance between the inferred original topography and the energy slope line (m), $v_{\max}$ is the maximum velocity (m/s), and g is gravitational acceleration (m/s^2; Hungr et al., 2005; Hungr, 2006; Hutchinson, 2006). If the sliding rock masses were saturated and pore water pressures were important, Eq. (1) will overestimate the maximum velocity because it ignores turbulent effects (Hungr et al., 2005). As such, the results produced by Eq. (1) should be considered maximum possible estimates. Note that $z_{\max}$ is not the difference between the scarp crest elevation and maximum run-up elevation. The use of that or other *Fahrböschung*-related $z_{\max}$ values can greatly overestimate velocity (Hutchinson, 2006). *Fahrböschung* angles are, however, included in this paper because of their historical persistence.

Slip surface dips were estimated from slope angle maps and the cross-sections produced from the digital elevation models; they are shown as apparent dips in the cross-sections because it was not always possible to draw the profiles exactly perpendicular to topographic contours. In each case, the slip surface dip was calculated assuming that the mountain-scale planar discontinuities observed today acted as sliding surfaces. Slope angles calculated from digital elevation models can underestimate the true slope for components of the topography with wavelengths shorter than twice the distance over which the slope is calculated. For a standard second-order accurate finite difference approximation, that distance is twice the digital elevation model grid spacing. For longer wavelength components of the topography, slopes estimated from digital elevation models can either overestimate or underestimate the true slope (Haneberg, 2006). Thus, we expect no systematic underestimation of slope angles for measurements of mountain- or valley-scale slopes made over distances of 180 m (which is twice the spacing of the original SRTM digital elevation models).

The geometry of the four landslides follows general trends established by previous authors, but with some differences. Fig. 10A shows that the *Fahrböschung* decreases exponentially as debris volume increases, although the landslides described in this paper, and particularly the Darcha landslide, depart from the well-known empirical relationship first published by Scheidegger (1973). Likewise, the logarithm of the planimetric area of the debris (A) increases proportionally to the logarithm of the debris volume (V) following the relationship:

$$\log_{10} A = 1.05 + 0.65 \log_{10} V \left(r^2 = 0.99,\ p = 0.0045\right) \quad (2)$$

in which A and V are in m^2 and m^3, respectively. The standard errors of the estimates are 0.35 for the intercept and 0.044 for the slope. Eq. (2) was obtained using standard least-squares linear regression for consistency with Iverson (2006). Fitting a line using reduced major axis regression yields results that are essentially indistinguishable, as would be expected from the very nearly collinear data (Haneberg, unpublished data). The implication of Eq. (2) is that the four landslides are substantially thicker relative to their areas than those used to establish the relationships described by Iverson (2006). Field observations such as stream incision across the Patseo landslide deposit suggest that our thickness estimates are reasonable. The reason for the greater thickness is unclear, but may be related to the steep terrain and narrow valleys into which the debris flowed. Both the Scheidegger (1973) and Iverson (2006) empirical models were derived from landslides over various topographic settings.

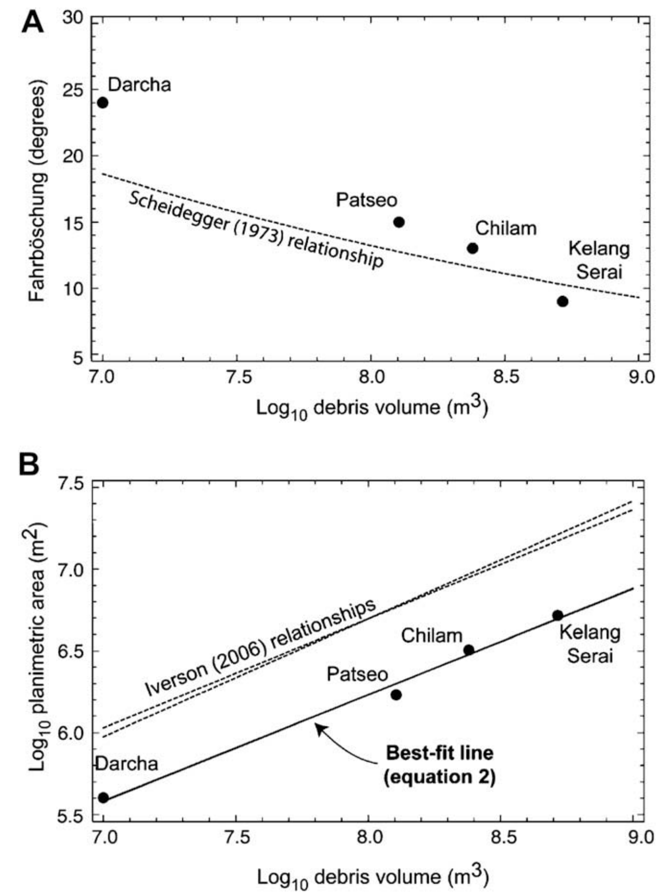

Fig. 10. Relationships between (A) landslide debris and Fahrböschung, and (B) surface area for the large landslides examined in this study.

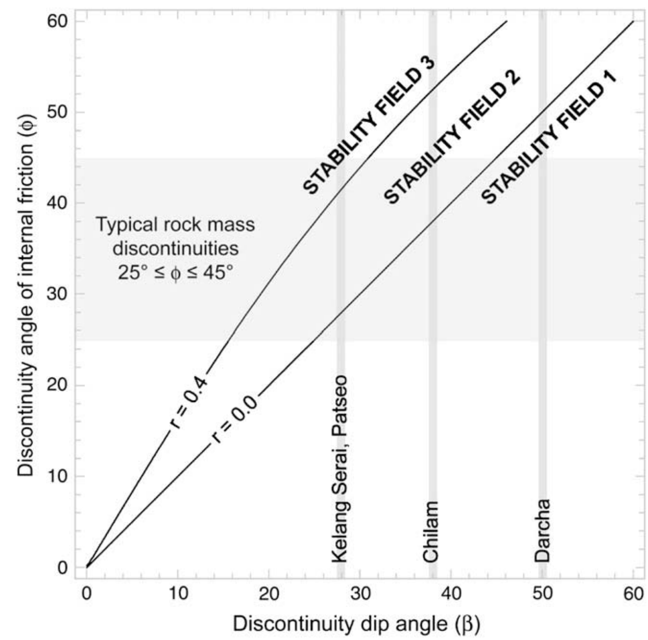

Fig. 11. Large landslides examined in this study plotted on idealized stability fields for frictional block sliding based on discontinuity dip and angle of internal friction. Stability field 1 is unconditionally unstable; stability field 2 can be destabilized by an increase in pore-water pressure during seismic shaking; and stability field 3 requires seismic shaking for destabilization.

7. Discussion

7.1. Slope stability and potential causes of sliding

Although we have no information about the strength of rock mass discontinuities, pore water pressures, or possible earthquakes at the time any of the four landslides occurred, we can make some informed speculations based on the mechanics of a highly idealized sliding block model. The factor of safety against sliding, which is the ratio of resisting to driving forces, for an infinite slope or rigid block resting on a planar discontinuity can be easily shown from first principles to be

$$FS = (1-r)\frac{\tan\varphi}{\tan\beta} \tag{3}$$

where r is a pore- or cleft-water pressure coefficient reflecting the reduction in normal stress arising due to saturation (dimensionless), φ is the angle of internal friction along the potential slip surface, and β is the dip of the potential slip surface (Haneberg, 2000). Cohesion along discontinuities is ignored in this simple analysis. For non-artesian conditions and typical rock densities, $0 \leqslant r \leqslant 0.4$, with the larger value reflecting complete saturation to the ground surface and slope-parallel flow. Angles of internal friction for rock mass discontinuities depend on the nature of the discontinuity and lithology, but very generally, $25^\circ \leqslant \varphi \leqslant 45^\circ$. This basic information can be used to define three stability fields (Fig. 11). Combinations of φ and β that plot within stability field 1 represent slopes that are unconditionally unstable if the dip of the discontinuities is less than the topographic slope. Slopes that plot within stability field 1 that have the discontinuities dipping more steeply than the topographic slope may fail by mechanisms such as toppling or buckling, but should not fail by frictional sliding. Combinations that plot within stability field 2 indicate slopes in which frictional sliding can be triggered by elevated pore water pressures, seismic acceleration, or a combination of the two processes. Long-term reduction of any cohesive strength that may exist, for example by slow movement in response to toe erosion, may also contribute to instability by reducing shear strength from peak to residual values. Slopes that plot within stability field 3 cannot be destabilized by pore water pressure alone; therefore, additional driving forces such as seismic shaking must exist for frictional block sliding to occur.

Comparison of the observed slip surface dips with typical angles of internal friction suggest that the Kelang Serai, Patseo, and Chilam landslides could have been triggered by increased pore water pressure, seismic shaking, or some combination of the two. The likelihood that increased pore water pressure alone could have triggered any of those landslides depends on the actual angle of internal friction and the existence of any cohesive strength along the slip surfaces, both of which are impossible to further quantify at this level of investigation. The Chilam landslide, which falls completely within stability field 2, could have been triggered by increased pore water pressure alone with values of r no higher than 0.2. The Kelang Serai and Patseo landslides could have likewise been triggered by increased pore water pressures alone if $\varphi \leqslant 40^\circ$ but would have required seismic shaking if $\varphi > 40^\circ$ or if cohesive strength was appreciable. This is not to say that seismicity did not or could not have triggered any of the four landslides, but only that it was not necessary unless $\varphi > 40^\circ$ for the Kelang Serai or Patseo landslides. One possibility is that increased pore water pressure may have reduced the intensity of seismic shaking necessary to trigger any or all of the landslides. The Darcha landslide, however, falls well within stability field 1. Field observations show that the rock mass discontinuities dip more steeply than the surrounding topography, therefore, movement by frictional block sliding is unlikely. Instead, other mechanisms such as gravitationally induced buckling and cracking of steeply dipping slabs bounded by discontinuities must be considered. Gravitationally induced buckling is consistent with the slight topographic irregularity apparent in the Darcha cross-section (Fig. 12), which may reflect the development of an oblique shear fracture as a consequence of buckling.

7.2. Causes of landslides

The data that we compiled on 12 dated large landslides in the Himalaya, together with the four investigated in this study, provide context for a discussion of the timing of sliding and trigger mechanisms in the Himalaya (Table 2; Fig. 1). All 12 of the landslides we

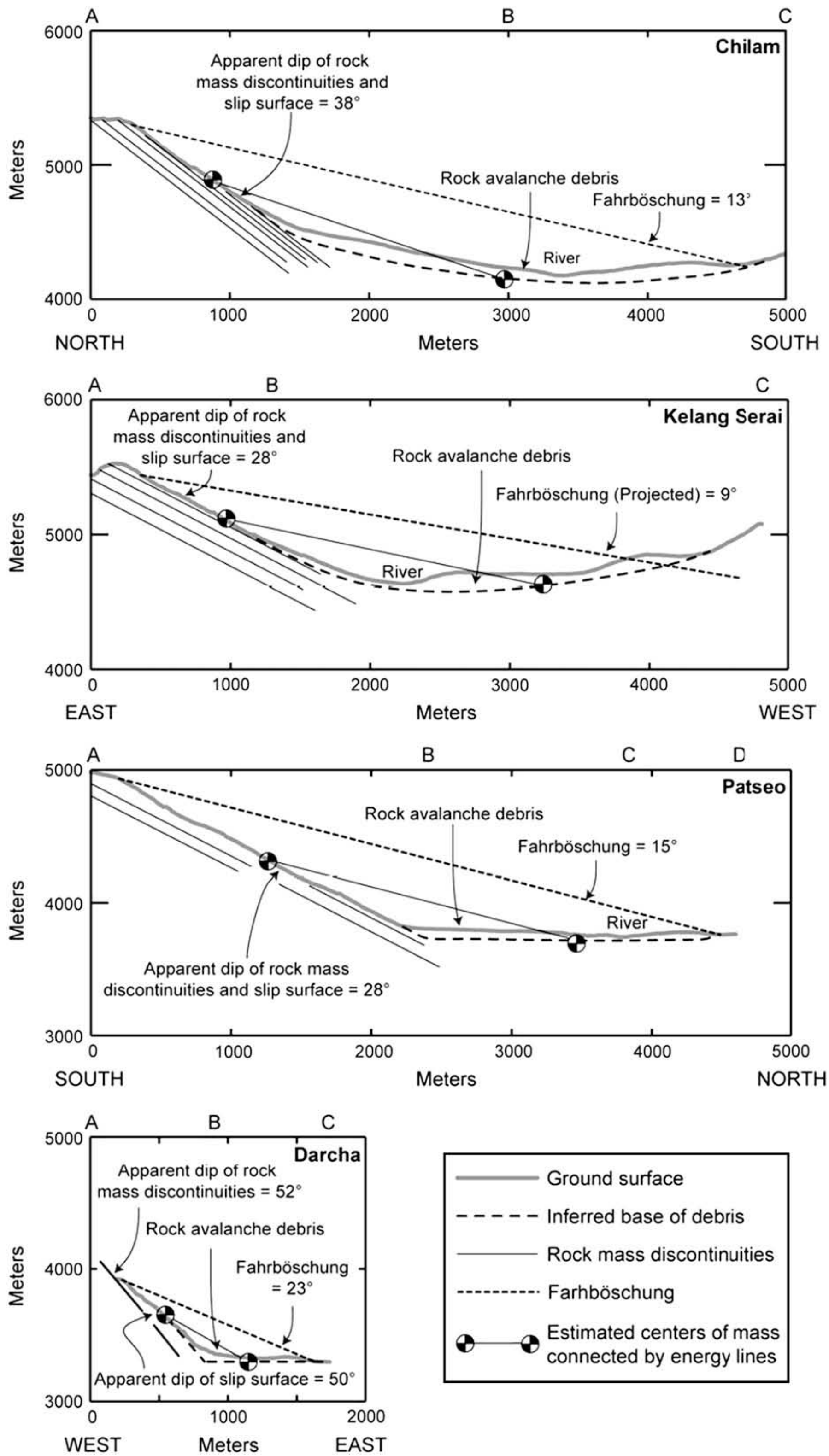

Fig. 12. Profiles of deposits and slope characteristics for the (A) Chilam, (B) Kelang Serai, (C) Patseo, and (D) Darcha landslides.

compiled are deep-seated bedrock landslides. Numerical dating shows that there are three clusters of ages: ~3 ka (two landslides), 6–14 ka (eleven landslides), and 31–34 ka (three landslides). These landslides can be attributed to causes (factors that make slopes conducive to landsliding) and triggers (factor that initiate landsliding). In this region the main causes are geologic structure, glacial debuttressing, and long-term increased precipitation, while the main triggers are heavy rainstorms and seismic shaking (Hewitt, 1988; Bookhagen et al., 2005; Dunning et al., 2007; Mitchell et al., 2007).

7.2.1. Structure

Local lithology, structure, and tectonic deformation can play a major role in preparing rock-slopes for large landslides (Weidinger et al., 2002). For example, they suggested the Darcha headscarp was predisposed to landsliding because of the structure and lithology of the mountain flank. Specifically, Weidinger et al. (2002) suggest that steep folding and transversal schistosity in laminated rocks, discordant dikes of metadiabase and metagabbro, and subsequent differential internal tension/mechanical behavior made the slope more susceptible to landsliding. Similarly, the Patseo headscarp syncline contains shear zones between ridged dolomites and ductile fine-grained sediments and discordant ore structures that likely reduced the strength of the rock-slope and promoted landsliding (Weidinger et al., 2002). Weidinger et al. (2002) also suggest the northeast-trending recumbent megafold oriented bedding of various lithologies into an orientation conducive to landslidng near the Kelanh Serai landslide. The Chilam headscarp is located in the Pangong Range and is composed of heavily fractured, deformed diorite and volcanics (Dunlap et al., 1998). These fractures likely weakened the rock-slope and enabled the generally planar scar to form. These tectonic structures likely enabled rock-slopes to destabilize more easily by heavy precipitation or seismic shaking and are a preparatory cause of the four large landslides investigated in this study.

7.2.2. Debuttressing

Debuttressing during deglaciation may alter topography-induced stress fields, focusing tensile stresses near valley floors, and promoting catastrophic movement (Haneberg, 1999; Korup et al., 2007). Debuttressing due to deglaciation or to glacial or fluvial incision can destabilize some slopes. Ballantyne (1995, 2002, 2004), Ballantyne and Benn (1994) emphasizes the importance of landsliding as a paraglacial process in landscapes during and after deglaciation. Most of the 300 landslides investigated by Korup et al. (2007), for example, occurred in deeply incised and formerly glaciated valleys. Of the 50 historic landslides cataloged by Keefer (1984), all but one occurred on slopes that were undercut by fluvial or glacial processes in the Late Quaternary. The Ghoro Choh landslide, for example, has been directly attributed to debuttressing (Seong et al., 2008; Shroder, in press).

The main valleys in the Lahul Himalaya, which contain the Darcha, Patseo, and Kelang Serai landslides, were deglaciated by the Early Holocene (Owen et al., 2001). The ^{10}Be ages on landslides investigated in this study indicate that they occurred between 6 and 8 ka, 2–4 ka after deglaciation, which suggests that glacial debuttressing was not the trigger. However, there may be a time lag between rock-slope instability and deglaciation. This would likely result in younger landslides being positioned further up valley than older landslides. However, there is no correlation between landslide age and position in the catchment for the ancient landslides compiled in this study. The lack of correlation is highlighted by the Dear landslide (10.2$\pm$0.6 ka) occurring ~5 km up stream of the Rangatoli landslide (3.0$\pm$0.1 ka). Glacial debuttressing, however, may be a preparatory cause of the Darcha, Patseo, and Kelang Serai landslides enabling rock-slopes to destabilize more easily by a heavy precipitation or seismic shaking.

7.2.3. Monsoon precipitation

The view that heavy precipitation can cause catastrophic sliding is generally accepted (Owen, 1991; Owen et al., 1995, 1996; Barnard et al., 2001; Bookhagen et al., 2005). Bookhagen et al. (2005) suggested that strengthened monsoon circulation in India during the Holocene caused several large landslides in the Sutlej River region of the Himalaya. They argued, based on paleoenvironmental evidence, that intensified monsoon phases during the Holocene occurred in many regions of monsoon Asia including the northwest Himalaya, Tibet, south China, Nanga Parbat, the southern portion of the Arabian Peninsula, and the Bay of Bengal. During these intensified monsoon phases, moisture penetrated more than 75 km beyond the orographic barrier (mountain ridges at >4500 m asl) in the Greater Himalaya (Bookhagen et al., 2005). An intensified monsoon phase could cause a steady rise of the water table and increase in cleft-water pressure creating conditions conducive to deep-seated landsliding. The bedrock of the four large landslides investigated here is heavily fractured and the fractures, bedding, and discordant intrusions are interconnected. The water in the fissures could exert a buoyant force and enable the rock-slope to destabilize more easily.

Even though the precise role of precipitation in deep-seated bedrock destabilization is unknown, several large landslides have been attributed to heavy precipitation. Bookhagen et al. (2005), for example, suggest that 13 large landslides ($>500\times10^6$ m^3) occurred during intensified monsoon phases in the late Pleistocene at or after 28.8 ka and in Holocene between 8.8 and 4 ka. Five of the 13 are included in our compilation of landslides of known age in Table 2. The remaining 8 have not been dated.

Shi et al. (2001) show that lake levels in Tibet were typically higher between 30 and 40 ka using terraces, cores, and pollen from seven lakes (including Pangong Tso). Also, using $^{18}\delta$ variation from two ice cores, they show that there was ~40–100% more precipitation than today. They attribute the higher lake levels and increased precipitation to an exceedingly strong summer monsoon climate over the Tibetan plateau.

Radiocarbon dating on sediment cores taken from Pangong Tso (Bangong Co) near the Chilam landslide, and from Sumxi-Longmu Co indicate three significant periods of increased precipitation during the Holocene: Pangong Tso 10.7–9.6, 8.4–7.2, and 3.4–2.1 ka; and Sumxi-Longmu Co 11.3–9.5, 8.4–7.1, and 4.0–2.6 ka (Gasse et al., 1991, 1996). Gasse et al. (1996) suggest that the Holocene maximum precipitation occurred between 8.4 and 7.2 ka at Pangong Tso and between 8.4 and 7.1 ka at Sumxi-Longmu Co. However, the radiocarbon chronology of this core is controversial and may contain significant error (Bookhagen et al., 2006; Mitchell et al., 2007).

Of the 16 dated ancient, large landslides (four from in this study and 12 previously published), only two (Kelang Serai and Gomboro of Seong et al., 2008) do not have ages within one standard deviation of a period of increased monsoon activity (Fig. 13). Seven of them likely occurred during the most intense monsoon phase in the Holocene, from 8.4 to 7.2 ka (Gasse et al., 1996). The older cluster of three landslides (Shaso, Chango, and Tsergo Ri) occur during the period of enhanced monsoon proposed by Shi et al. (2001). All of the ancient landslides occur during times of Prell and Kutzbach (1987) increased monsoon pressure and precipitation. The correlation between large-landslide occurrence and times of strengthened monsoons and the limited landslide occurrence during times of decreased monsoon intensity suggests a causal link. However, the one sigma uncertainties in the landslide ages and the error in the modeled radiocarbon chronology of the Pangong Tso core by Gasse et al. (1996) make this link tentative.

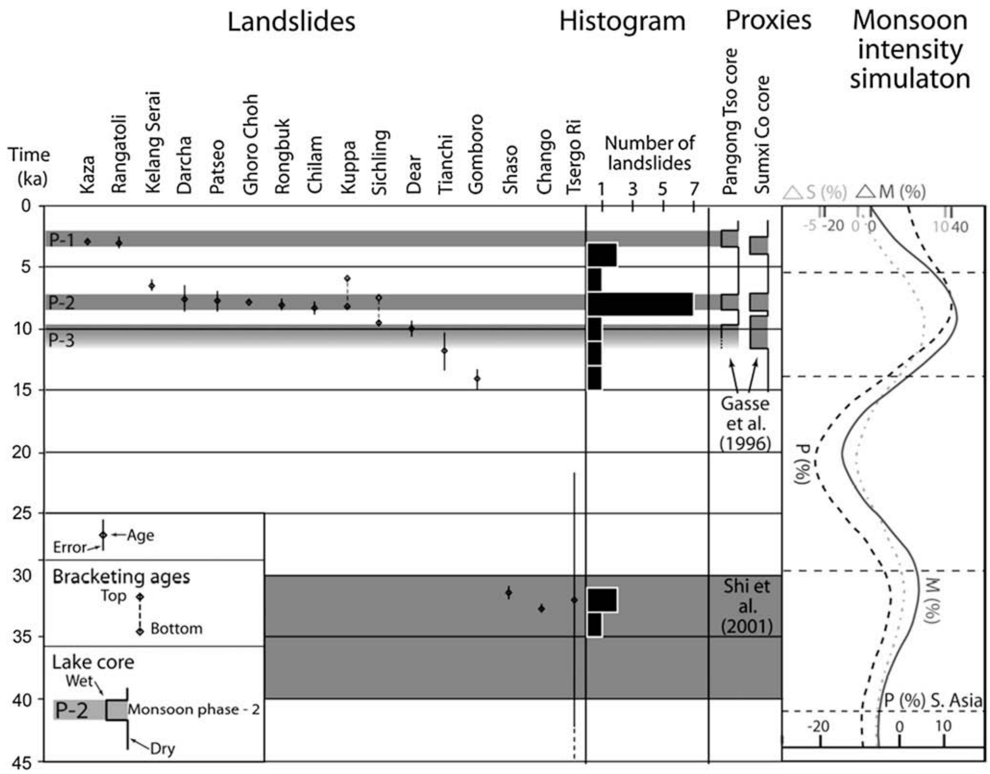

Fig. 13. Diagram illustrating relationships among landslides of known age and curves of monsoon intensity and precipitation based on lake cores. Thin gray intervals indicate enhanced monsoon phases and subsequent increased precipitation based on lake core data taken from Gasse et al. (1996). Error bars on landslide ages represent 2σ internal errors from statistical analysis. Histogram uses 2 ka bin width for landslide occurrence. Dashed horizontal lines on right side show maximum age ranges of rock avalanche clusters crossing the modeled monsoon intensity curve. Thick gray bar is period of enhanced monsoon precipitation between 30 and 40 ka inferred form lake terraces, pollen, lake cores, and ice cores by Shi et al. (2001). The three curves in the proxy data section show the simulated monsoon pressure index (ΔM percentage, solid line) for the Indian Ocean, simulated changes in precipitation (P percentage, thick black dashed line) in southern Asia, and variations in Northern Hemisphere solar radiation (ΔS percentage, thin gray dashed line) after Prell and Kutzbach (1987).

7.3. Landslide triggers

7.3.1. Heavy precipitation events

A heavy precipitation event, such as an intensified monsoon, can trigger a large-landslide in two ways: (1) destabilization of a slope through increased cleft-water pressure; and (2) subsequent flooding that rapidly removes significant amounts of sediment and undercuts and destabilizes a slope.

Heavily fractured bedrock composed of varying lithologies can weaken rock-slopes and enable intense rainstorm events to trigger large landslides, such as the Tatopani landslide (Volk, 2000). The two joint sets crossing each other and acting in conjunction with foliation as a shear plane, were responsible for a wedge failure of $0.4\times10^6\,m^3$ (Volk, 2000). The trigger was extreme and lengthy monsoon rainstorms, which reinforce the cleft-water pressure inside rock discontinuities along the impermeable interface of quartzites and phyllites at the base of the wedge failure (Volk, 2000). Historic large landslides also have been triggered by heavy monsoon precipitation. Hewitt (1988), for example, reported 3 rock avalanches (Bualtar 1, 2, and 3) on the Bualtar Glacier in 1986 that were triggered by precipitation.

Enhanced monsoon precipitation can increase sediment flux and flood frequency (Bookhagen et al., 2005). Erosion by floods likely widens rather than incises channels in areas where the bedrock is fractured or jointed, which can undercut and destabilize rock-slopes (Hartshorn et al., 2002). However, removal of transiently stored material in the channel can also be a landslide trigger. During the Early Holocene intensified monsoon period, the increased moisture supply may have removed material from the valleys and stored it farther downstream (Bookhagen et al., 2006). Undercutting, significant removal of valley fills, and saturated rock-slopes may have triggered some of the landslides investigated in this study. Further investigation of the history of sediment removal and high precipitation events is needed to support this suggestion.

7.3.2. Ground shaking

Keefer (1984, 1994) highlighted the importance of seismic shaking as a trigger for a variety of landslides, including large rock avalanches, and showed that even small earthquakes ($M=4$) may initiate landslides. Earthquakes with moment magnitudes greater than 7.5 typically generate thousands to tens of thousands of small landslides, but few very large ones. The 2005 Kashmir earthquake, which had a magnitude of 7.6, generated several thousand landslides over an area of 7500 km^2, but only one landslide was $\sim10^6\,m^3$ (Dunning et al., 2007; USGS, 2006; Owen et al., 2007).

The 1991 and 1999 Garhwal earthquakes ($M_s=7.1$ and $M_s=6.6$, respectively) occurred in a similar geologic setting to the 2005 Kashmir earthquake but were smaller and did not trigger any large landslides (USGS, 2006; Owen et al., 2007). The $M_s=6.6$ earthquake in 1999 induced mass movements totaling $0.02\times10^6\,m^3$, equivalent to 0.09 mm/yr of landscape lowering (Barnard et al., 2001; USGS, 2006). Two of the largest 30 landslides recognized in Garhwal were triggered by the earthquake while the other 28 have been suggested to have been caused by precipitation (Barnard et al., 2001). Owen et al. (2007) suggest that an earthquake magnitude threshold may exist for widespread landsliding such as occurred in Kashmir, consistent with Keefer's (1994) suggestion that earthquakes must exceed M 7.5 to induce large-scale landsliding. The above evidence suggests that moderate earthquakes ($M\leqslant7.5$) are unlikely to trigger large landslides (Owen et al., 2007).

A large ($M>7.5$) earthquake could trigger a large-landslide, but there are few studies that demonstrate this as an effective trigger. Weidinger et al. (in press) suggests that a giant ($400\times10^6\,m^3$) rock avalanche near Kanchenjunga was triggered by an earthquake, although there is no independent evidence for an earthquake trigger. The lack of paleoseismic evidence, however, is not proof of the absence of seismic activity. Historical seismic activity such as the 1991 Garhwal and 2005 Kashmir earthquakes underline that the Himalaya are seismically active and that earthquakes can induce large-mass movements. Moreover, more than 11 earthquakes with $M\geqslant7.5$ have occurred in the Himalaya since 1720 A.D. (Bilham et al., 2001). Several $M\geqslant7.5$ earthquakes occurring in study area within a 1 ka interval, such as during an intensified monsoon phase, is possible.

7.4. Summary

The valleys in which the Darcha, Patseo, and Kelang Serai landslides occurred were deglaciated >2 ka before landsliding. Also, younger landslides are not generally found further up their catchments. This suggests that glacial debuttressing was not the trigger of the landsliding. Glacial debuttressing and glacial or fluvial incision, however, may be important in conditioning slopes to subsequent failure. The consistent presence of tectonic structures suggests that they may be necessary to weaken rock-slopes for large landslides to occur.

The temporal association between the occurrence of large landslides and enhanced monsoon precipitation suggests that the latter plays an important role in triggering large landslides. The heavily fractured bedrock and varying lithologies could have enabled an enhanced monsoon rainstorm to trigger any of the four large landslides investigated in this study. Enhanced precipitation may also have removed transiently stored material in the channel and undercut rock-slopes causing destabilization. Proving that precipitation is the trigger is not possible without better understanding of the role played by increased pore pressure in bedrock slopes and a more established chronology of the Pangong Tso and Sumxi-Longmu Co cores.

Seven landslides (Darcha, Patseo, Ghoro Choh, Rongbuk, Chilam, Kuppa, and Sichling) have ages that are within 1 sigma error of each other. Unfortunately, the accuracy of ^{10}Be dating is not high enough to determine if they occurred at the same time. The combined effects of antecedent debuttressing, heavy precipitation, and seismic shaking should be emphasized. Long-term increases in precipitation may have increased steady-state or background pore water pressures to the point that some previously resistant slopes could be destabilized by seismic shaking. Seismic ground shaking can be amplified on ridges, shatter bedrock, and reduce rock strength, possibly enabling later precipitation during the monsoon season to push a slope beyond its stability threshold (Owen et al., 2007). Conversely, heavy precipitation can reduce the seismic acceleration necessary to trigger a landslide. Seismic activity during one of the intense monsoon phases may thus be responsible for many of the large landslides reported in this paper. More investigation is needed to test whether this interplay of factors caused the ancient landslides reported here.

7.5. Geomorphic importance

Landslide erosion rates are needed for comparison with fluvial and glacial erosion rates in order to determine their relative importance in landscape evolution. The temporal clustering of landslides, especially those that cluster around the monsoon phase at 8.4–7.2 ka, makes erosion rate estimates heavily dependent on the time scale used. Therefore, we standardize for an interglacial time period (the Holocene) to make our rates easily comparable with future investigations. Moreover, it is difficult to account for the volume of thousands to hundreds of thousands of small landslides. The large-landslide volumes, however, can be used to define minimum erosion rates caused by mass movement. Owen et al. (1996) and Barnard et al. (2001) suggest that the large landslides are much more significant volumetrically and have much higher preservation potential for a given background erosion rate compared to the many small ones. Investigation of 338 mass movements by Barnard et al. (2001) show that the largest three landslides account for $\sim3.6\times10^{-4}$ mm/yr of the 5.7×10^{-4} mm/yr landscape lowering and represent 62% of the total volume of landslide debris produced.

Korup et al. (2007) suggest that erosion due to giant landslides during the Late Pleistocene and Holocene in the Himalaya is $\leqslant4.2\pm0.2$ mm/yr. Barnard et al. (2001) show that landsliding in the Garhwal is equivalent to 57.0×10^{-3} mm/yr of landscape lowering during the Holocene. Keefer (1994) suggests that landslides contributed $\sim5.0\times10^{-3}$ mm of ground-surface lowering on slopes in Tibet from 715 A.D. to the present resulting in 0.007×10^{-3} mm/yr of slope lowering during the latest Holocene. The lower Holocene rates may indicate a decreased contribution from large landslides since the Late Pleistocene. They may, however, reflect the lack of identified mass movements and/or the paucity of studies.

Estimates of landslide erosion rates are problematic due to differences in basin size, relief, hypsometry, and the length of landslide record. To make a regional assessment and average out single basin uncertainties, numerous mass movement volumes throughout a geographic region during a significant time period, such as the Holocene, need to be calculated. This will also enable the validity of the landslide volume/catchment size landscape-lowering method to be tested. The number of dated large landslides of known volume, however, is limited; thus a regional assessment is impossible at this time. We can, however, provide single catchment erosion rates for large landslides.

A net landscape-lowering rate of ~0.015 mm/yr was calculated for the combined Darcha and Patseo catchment. The net landscape lowering of the Patseo landslide alone is ~0.035 mm/yr and is higher than the combined Darcha-Patseo rate due to the much smaller catchment. The net landscape-lowering rate for the Kelang Serai catchment is ~0.32 mm/yr. This rate is an order of magnitude larger than the Darcha, Patseo, and Chilam landslides, due to the smaller catchment size and the large volume of the Kelang Serai landslide. The landscape-lowering rate for the Chilam landslide is $<10^{-3}$ mm/yr. The deposit is located in the Loi Yogma valley, which contains the main trace of the Karakoram Fault and results in a very large catchment. The average landscape lowering due to large landslides for the region of Lahul that contains the Darcha, Patseo, and Kelang Serai landslides is ~0.12 mm/yr. Differences between our landscape-lowering rates and those of Keefer (1994), Barnard et al. (2001), and Korup et al. (2007) highlight the problems of using single basin calculations and the need for regional landscape lowering determinations. More studies like ours will enable the contribution of Himalayan mass movements to regional denudation to be determined in the future.

8. Conclusions

Four large landslides were mapped and successfully dated. The weighted mean ^{10}Be ages of the Darcha (7.7 ± 1.0 ka), Patseo (7.9 ± 0.8 ka), Kelang Serai (6.6 ± 0.4), and Chilam (8.5 ± 0.5 ka) landslides have MSWD<1 indicating that each set of sampled blocks represents one population. This is, of course, within the statistically reliable temporal resolution of ^{10}Be dating. The similarity of the Darcha, Patseo, and Chilam ages raises the possibility, but does not prove that the landslides occurred at the same time. Bedrock discontinuities in the headscarp of the Darcha landslide dip at a steeper angle than the topographic slope, indicating that the slope is conditionally stable with respect to frictional block sliding. This landslide may have been triggered by gravitationally induced buckling and cracking of steeply dipping slabs bounded by discontinuities. Comparison of slip surface dips and angles of internal friction suggests that the Patseo, Kelang Serai, and Chilan landslides were likely triggered by high pore water pressure, seismic shaking, or a combination of the two. We suggest that strengthened monsoons play an important role in triggering large landslides in our study due to the association of landslide ages and times of strengthened monsoon. This coincidence, however, does not preclude a seismic trigger.

Average landscape lowering for the region of Lahul that contains the Darcha, Patseo, and Kelang Serai landslides is ~0.12 mm/yr. Differences between landscape-lowering rates in our study area compared to those in other mountain ranges in the Himalayan–Tibetan orogen highlight the importance of catchment size and the need for more studies of the type reported here to accurately estimate regional landscape lowering by mass movement processes.

Acknowledgments

We thank Oliver Korup for discussions regarding the location and nature of giant landslides in the Himalaya, Susan Ma at PRIME Lab for developing the Rock Age calculator and helping to calculate the ^{10}Be ages, Kate Hendrick for helping to prepare samples 2 to 9, and Tim Phillips for drafting Figs. 2 and 6. Special thanks to Dr. Weidinger and Dr. Bookhagen for their constructive and very detailed reviews of this paper.

References

Balco, G., Briner, J., Finkel, R.C., Rayburn, J., Ridge, J.C., Schaefer, J.M., 2008. Regional beryllium-10 production rate calibration for late-glacial northeastern North America. Quaternary Science Reviews, submitted.

Ballantyne, C.K., 1995. Paraglacial debris cone formation on recently deglacited terrain. The Holocene 5, 25–33.

Ballantyne, C.K., 2002. Paraglacial geomorphology. Quaternary Science Reviews 21, 1935–2017.

Ballantyne, C.K., 2004. Paraglacial landsystems. In: Evans, D.J. (Ed.), Glacial Landsystems. Edward Arnold, London, pp. 432–461.

Ballantyne, C.K., Benn, D.I., 1994. Paraglacial slope adjustment and resedimentation following recent glacier retreat, Fabergstolsdalen, Norway. Arctic and Alpine Research 26, 255–269.

Barnard, P.L., Owen, L.A., Sharma, M.C., Finkel, R.C., 2001. Natural and human-induced landsliding in the Garhwal Himalaya of Northern India. Geomorphology 40, 21–35.

Barnard, P.L., Owen, L.A., Sharma, M.C., Finkel, R.C., 2004. Late Quaternary landscape evolution of a monsoon-influenced high Himalayan valley, Gori Ganga, Nanda Devi, NE Garhwal. Geomorphology 61, 91–110.

Barnard, P.L., Owen, L.A., Finkel, R.C., 2006. Quaternary fans and terraces in the Khumbu Himal south of Mount Everest: their characteristics, age and formation. Journal of Geological Society of London 163, 383–399.

Benn, D.I., Owen, L.A., 2002. Himalayan glacial sedimentary environments: a framework for reconstructing and dating former extents of glaciers in high mountains. Quaternary International 97/98, 3–26.

Bhattacharyya, A., 1989. Vegetation and climate during the last 30,000 years in Ladakh. Palaeogeography, Palaeoclimatology, Palaeoecology 73, 25–38.

Bilham, R., Gaur, V.K., Molnar, P., 2001. Himalayan seismic hazard. Science 293, 1442–1444.

Bookhagen, B., Thiede, R.C., Strecker, M.R., 2005. Late Quaternary intensified monsoon phases control landscape evolution in the northwest Himalaya. Geology 33, 149–152.

Bookhagen, B., Thiede, R.C., Strecker, M.R., 2006. Late Quaternary intensified monsoon phases control landscape evolution in the northwest Himalaya. Geological Society of America 33, 149–152.

Brown, E.T., Bendick, R., Bourlés, D.L., Gaur, V., Molnar, P., Raisbeck, G.M., Yiou, F., 2003. Early Holocene climate recorded in geomorphological features in western Tibet. Palaeogeography, Palaeoclimatology, Palaeoecology 199, 141–151.

CGIAR-CSI, 2007. The CGIAR Consortium for Spatial Information. ⟨http://srtm.csi.cgiar.org/SELECTION/inputCoord.asp⟩.

Derbyshire, E., 1983. The Lushan dilemma: Pleistocene glaciation south of the Chang Jiang (Yangtze River). Zeitschrift für Geomorphologie 27, 445–471.

Derbyshire, E., 1996. Quaternary glacial sediments, glaciation style, climate, and uplift in the Karakoram and Northwest Himalayas: review and speculations. Palaeogeography, Palaeoclimatology, Palaeoecology 120, 147–157.

Derbyshire, E., Owen, L.A., 1990. Quaternary alluvial fans in the Karakoram Mountains. In: Rachocki, A.H., Church, M. (Eds.), Alluvial Fans: a Field Approach. Wiley, Chichester, pp. 27–53.

Derbyshire, E., Owen, L.A., 1997. Quaternary glacial history of the Karakoram Mountains and Northwest Himalayas: a review. Quaternary International 38/39, 85–102.

Desilets, D., Zreda, M., 2003. Spatial and temporal distribution of secondary cosmic-ray nucleon intensities and applications to in situ cosmogenic dating. Earth and Planetary Science Letters 206, 21–42.

Dunlap, W.J., Weinberg, R.F., Searle, M.P., 1998. Karakoram fault zone rocks cool in two phases. Geological Society of London 155, 903–912.

Dunning, S.A., Mithcell, W.A., Rosser, N.J., Petley, D.N., 2007. The Hattian Bala rock avalanche and associated landslides triggered by the Kashmir Earthquake of 8 October 2005. Engineering Geology 93, 130–144.

Fort, M., 1986. Glacial extension and catastrophic dynamics along the Annapurna Front, Nepal Himalaya. Göttinger Geographische Abhandlungen 81, 105–125.

Fort, M., 1988. Catastrophic sedimentation and morphogenesis along the High Himalayan Front, implications for palaeoenvironmental reconstructions. In: Whyte, P., Aigner, J.S., Jablonski, N.G., Taylor, G., Walker, D., Wang, P. (Eds.), The Palaeoenvironment of East Asia from Mid-Tertiary. Proceedings of the Second International Conference, Centre of Asian Studies Occasional Papers and Monographs 77. University of Hong Kong, pp. 170–194.

Fort, M., 1989. The Gongba conglomerates: glacial or tectonic? Zeitschrift für Geomorphologie 76, 181–194.

Fort, M., 1995. The Himalayan glaciation: myth and reality. Journal of Nepal Geological Society 11 (Special Issue), 257–272.

Fort, M., 1996. Late Cenozoic environmental changes and uplift on the northern side of the central Himalaya: a reappraisal from field data. Palaeogeography, Palaeoclimatology, Palaeoecology 120, 123–145.

Fort, M., 2003. Are high altitude, lava stream-like, debris mixtures all rock glaciers? A perspective from the Western Himalaya. Zeitschrift für Geomorphology 130, 11–29.

Fort, M., Derbyshire, E., 1988. Some characteristics of tills in the Annapurna Range, Nepal. In: Whyte, P., Aigner, J.S., Jablonski, N.G., Taylor, G., Walker, D., Wang, P. (Eds.), The Palaeoenvironments of East Asia from Mid-Tertiary. Proceedings of the Second International Conference. Centre of Asian Studies Occasional Papers and Monographs, Geology, Sea level Changes, Palaeoclimatology and Palaeobotany 1. University of Hong Kong, pp. 195–214.

Fuchs, G., Linner, M., 1995. Geological traverse acrossthe western Himalaya—a contribution to the geology of eastern Ladakh, Lahul, and Chamba. Gjahrbuch Der Geologischen Bundesanstalt 138, 655–685.

Gasse, F., Arnold, M., Fontes, J.C., Fort, M., Gilbert, E., Huc, A., Bingyan, L., Yuanfang, L., Qing, L., Melleres, F., Van Campo, E., Fubao, W., Qingsong, Z., 1991. A 13,000-year climate record from western Tibet. Nature 353, 742–745.

Gasse, F., Fontes, J.C., Van Campo, E., Wei, K., 1996. Holocene environmental changes in Bangong Co basin (Western Tibet). Part 4: discussion and conclusions. Paleogeography, Paleoclimatology, Paleoecology 120, 79–92.

Gilchrist, A.R., SummerWeld, M.A., Cockburn, H.A.P., 1994. Landscape dissection, isostatic uplift, and the morphologic development of orogens. Geology 22, 963–966.

Haneberg, W.C., 1999. Effects of valley incision on the subsurface state of stress—theory and application to the Rio Grande valley near Albuquerque, New Mexico. Environmental and Engineering Geoscience 5, 117–131.

Haneberg, W.C., 2000. Deterministic and probabilistic approaches to geologic hazard assessment. Environmental and Engineering Geoscience 6, 209–226.

Haneberg, W.C., 2006. Effects of digital elevation model errors on spatially distributed seismic slope stability calculations: an example from Seattle, Washington. Environmental and Engineering Geoscience 12, 247–260.

Haneberg, W.C., 2007. Using airborne LiDAR and GIS technologies for field verified virtual landslide hazard mapping—a new approach to an old problem with examples from Papua New Guinea and San Francisco. Geological Society of America Abstracts with Program 39, 439.

Haneberg, W.C., Creighton, A.L., Medley, E.W., Jonas, D.A., 2005. Use of LiDAR to assess slope hazards at the Lihir gold mine, Papua New Guinea. In: Hungr, O., Fell, R., Couture, R., Eberhardt, E. (Eds.), Landslide Risk Management. Proceedings of International Conference on Landslide Risk Management, Vancouver, Canada, 31 May–3 June, 2005, Supplementary CD.

Hartshorn, K., Hovius, N., Dade, B., Slingerland, R.L., 2002. Climate-driven bedrock incision in an active mountain belt. Science 297, 2036–2038.

Heim, A., 1932. Bergsturz und Menschenleben. Fretz and Wasmuth, Zurich. 218pp.

Hewitt, K., 1988. Catastrophic landslide deposits in the Karakoram Himalaya. Science 242, 64–67.

Hewitt, K., 1998. Catastrophic landslides and their effects on the Upper Indus streams, Karakoram Himalaya, northern Pakistan. Geomorphology 26, 47–80.

Hewitt, K., 1999. Quaternary moraines vs catastrophic rock avalanches in the Karakoram Himalaya, Northern Pakistan. Quaternary Research 51, 220–237.

Hewitt, K., 2002. Styles of rock avalanche depositional complexes conditioned by very rugged terrain, Karakoram Himalaya, Pakistan. In: Evans, S.G., Degraff, J. (Eds.), Catastrophic Landslides: effects, Occurrence and Mechanisms. Geological Society of America Reviews in Engineering Geology, pp. 345–377.

Hungr, O., 2006. Rock avalanche occurrence, process, and modeling, In: Evans, S.G., Mugnozza, G.S., Strom, A., Hermanns, R.L. (Eds.), Landslides from Massive Rock Slope Failure. Proceedings of the NATO Advanced Research Workshop on

Massive Rock Slope Failure: new Methods for Hazard Assessment, Celano, Italy, 16–21 June 2002, pp. 243–266.
Hungr, O., Coromina, J., Eberhardt, E., 2005. Estimating landslide motion mechanism, travel distance and velocity. In: Hungr, O., Fell, R., Couture, R., Eberhardt, E. (Eds.), Landslide Risk Management. Taylor & Francis, London, pp. 99–128.
Hutchinson, J.N., 2006. Massive rock slope failure: perspectives and retrospectives on state-of-the-art. In: Evans, S.G., Mugnozza, G.S., Strom, A., Hermanns, R.L. (Eds.), Landslides from Massive Rock Slope Failure. Proceedings of the NATO Advanced Research Workshop on Massive Rock Slope Failure: new Methods for Hazard Assessment, Celano, Italy, 16–21 June 2002, pp. 619–662.
Iverson, R.M., 2006. Forecasting runout of rock and debris avalanches. In: Evans, S.G., Mugnozza, G.S., Strom, A., Hermanns, R.L. (Eds.),, Landslides from Massive Rock Slope Failure. Proceedings of the NATO Advanced Research Workshop on Massive Rock Slope Failure: new Methods for Hazard Assessment, Celano, Italy, pp., 197–209, 16–21 June 2002
Keefer, D.K., 1984. Landslides caused by earthquakes. Geological Society o America Bulletin 95, 406–421.
Keefer, D.K., 1994. The importance of earthquake-induced landslides to long-term slope erosion and slope-failure hazards in seismically active regions. Geomorphology 10, 265–284.
Korup, O., Strom, A.L., Weidinger, J.T., 2006. Fluvial response to large rock-slope failures: examples from the Himalayas, the Tien Shan, and the Southern Alps in New Zealand. Geomorphology 78, 3–21.
Korup, O., Clague, J.J., Hermanns, R.L., Hewitt, K., Strom, A.L., Weidinger, J.T., 2007. Giant landslides, topography, and erosion. Earth and Planetary Science Letters 261, 578–589.
Lal, D., 1991. Cosmic ray labeling of erosion surfaces; in situ nuclide production rates and erosion models. Earth and Planetary Science Letters 104, 424–439.
McDougall, I., Harrison, T.M., 1999. Geochronology and thermochronology by the 40Ar/39Ar method, second ed. Oxford University Press, Oxford. 269pp.
Mitchell, W.A., Dunning, S., Taylor, P.J., 2001. Preliminary investigation of rock avalanches in the Indian Himalaya. Journal of Asian Earth Sciences (Abstract Volume of the 16th HKTW workshop 2001, Schloss Seggau, Austria) 19, 3A. 45.
Mitchell, W.A., McSaveney, M.J., Zondervan, A., Kim, K., Dunning, D.A., Taylor, P.J., 2007. The Keylong Seri rock avalanche, NW Indian Himalaya: geomorphology and palaeoseismic implications. Landslides 4, 245–254.
NASA, 2007. National Aeronautics and Space Administration Land Processes Distributed Active Archive Center, Earth Observing Data Gateway. ⟨http://edcimswww.cr.usgs.gov/pub/imswelcome/⟩
Nishiizumi, K., Arnold, J.R., Klein, J., Kohl, C.P., Lal, D., Middleton, R., Winterer, E.L., 1989. Cosmic ray production rates of ^{10}Be and ^{26}Al in quartz from glacially polished rocks. Journal of Geophysical Research 94, 17907–17915.
Owen, L.A., 1991. Mass movement deposits in the Karakoram Mountains: their sedimentary characteristics, recognition and role in Karakoram landform evolution. Zeitschrift für Geomorphologie 35, 401–424.
Owen, L.A., Benn, D.I., Derbyshire, E., Evans, D.J., Mitchell, W.A., Thompson, D., Richardson, S., Lloyd, M., Holden, C., 1995. The geomorphology and landscape evolution of the Lahul Himalaya, Northern India. Zeitschrift fur Geomorphology 39, 145–174.
Owen, L.A., Sharma, M., Bigwood, R., 1996. Landscape modification and geoorphological consequences of the 20 October 1991 earthquake and the July–August 1992 monsoon in the Garhwal Himalaya. Zeitschrift fur Geomorphology 103, 359–372.
Owen, L.A., Mitchell, W., Bailey, R.M., Coxon, P., Rhodes, E., 1997. Style and timing of glaciation in the Lahul Himalaya, northern India: a framework for reconstructing late Quaternary palaeoclimatic change in the western Himalayas. Journal of Quaternary Science 12, 83–109.
Owen, L.A., Gualtieri, L., Finkel, R.C., Caffee, M.W., Benn, D.I., Sharma, M.C., 2001. Cosmogenic radionuclide dating of glacial landforms in the Lahul Himalaya, Northern India: defining the timing of Late Quaternary glaciation. Journal of Quaternary Science 16, 555–563.
Owen, L.A., Kamp, U., Khattak, G.A., Harp, E., Keefer, D.K., Bauer, M.A., 2007. Landslides triggered by the 8 October 2005 Kashmir earthquake, Geomorphology, in press.
Phartiyal, B., Sharma, A., Upadhyay, R., Ram-Awatar, Sinha, A.K., 2005. Quaternary geology, tectonics and distribution of palaeo- and present fluvio/glacio lacustrine deposits in Ladakh, NW Indian Himalaya—a study based on field observations. Geomorphology 65, 241–256.
Prell, W.L., Kutzbach, J.F., 1987. Monsoon variability over the past 150,000 yr. Journal of Geophysical Research 92, 8411–8425.
PRIME Laboratory, 2007. PRIME Laboratory rock age calculator. ⟨https://www.physics.purdue.edu/ams/rosetest/Rkversion1/rockpara.php⟩.
Scheidegger, A.I., 1973. On the prediction of the reach and velocity of catastrophic landslides. Rock Mechanics and Rock Engineering 5, 231–236.
Schramm, J.M., Weidinger, J.T., Ibetsberger, H.J., 1998. Petrologic and structural controls on geomorphology of prehistoric Tserog Ri slope failure, Langtang Himal, Nepal. Geomorphology 26, 107–122.
Seong, Y.B., Bishop, M.P., Bush, A., Clendon, P., Copland, L., Finkel, R., Kamp, U., Owen, L.A., Shroder, J.F., 2008. Landforms and landscape evolution in the Skardu, Shigar and Braldu valleys, central Karakoram. Geomorphology, in press.
Shi, Y., Yu, G., Liu, X., Li, B., Yao, T., 2001. Reconstruction of the 30–40 ka BP enhanced Indian monsoon climate based on geological records from the Tibetan Plateau. Paleogeography, Paleoclimatology, Paleoecology 169, 69–83.
Shroder, J.F., 1998. Slope failure and denudation in the western Himalaya. Geomorphology 26, 81–105.
Shroder, J.F., in press. Postglacial slope failure and denudation in the central Karakoram. Quaternary Science Reviews.
Small, E.E., Anderson, R.S., Repka, J.L., Finkel, R., 1997. Erosion rates of alpine bedrock summit surfaces deduced from in situ ^{10}Be and ^{26}al. Earth and Planetary Science Letters 150, 413–425.
Spotila, J.A., Buscher, J.T., Meigs, A.J., Reiners, P.W., 2004. Long-term glacial erosion of active mountain belts: example of the Chugach-St. Elias Range, Alaska. Geology 32, 501–504.
Steck, A., 2003. Geology of the NW India Himalaya. Eclogae Geologicae Helvetiae 96, 147–196.
Stone, J.O., 2000. Air pressure and cosmogenic isotope production. Journal of Geophysical Research 105, 23753–23759.
USGS, 2006. Earthquake Hazards Program. ⟨http://earthquake.usgs.gov/eqcenter/eqinthenews/2005/usdyae/⟩.
Volk, H.R., 2000. The 1998 Tatopani landslide in the Kali Gandaki Valley of western Nepal; cause and relation to mass rock creep. Journal of Nepal Geological Society 22, 405–412.
Wagner, G.A., 1995. Altersbestimmung von jungen Gesteinen und Artefakten: physikalische und chemische Uhren in Quartärgeologie nd Archäologie. Enke, Stuttgart. 277pp.
Walder, J.S., O'Connor, J.E., 1997. A rapid method for predicting peak discharge of floods caused by failure of natural and constructed earthen dams. Eos, Transactions, American Geophysical Union 78, 278.
Weidinger, J.T., 2006. Predesign, failure and displacement mechanisms of large rockslides in the Annapurna Himalayas, Nepal. Engineering Geology 83, 201–216.
Weidinger, J.T., Nuschej, F., 2001. Large-scale landslides along the Manali-Leh-Road (Northern India). Journal of Asian Earth Sciences (Abstract Volume of the 16th HKTW workshop 2001, Schloss Seggau, Austria), 19, 3A, addenda abstracts, 13–14.
Weidinger, J.T., Schramm, J., Surenian, R., 1996. On preparatory causal factors, initiating the prehistoric Tsergo Ri landslide (langthang Himal, Nepal). Tectonophysics 260, 95–107.
Weidinger, J.T., Ibetsberger, H.J., Nuschej, F., 2002. Hazard and risk in the reas of the rock avalanches of Darcha, Pateo and Sarai Kenlung (Manali-Leh-Road, Himachal Pradesh, India). Geoöko 23, 251–267. Bensheim.
Weidinger, J., Korup, O., in press. Frictionite as evidence for a large Late Quaternary rockslide near Kanchenjunga, Sikkim Himalayas, India—implications for extreme events in mountain relief destruction. Geomorphology, in press.
Yi, C., Zhu, L., Seong, Y.B., Owen, L.A., Finkel, R.C., 2006. A lateglacial rock avalanche event, Tianchi Lake, Tien Shan, Xinjiang. Quaternary International 154–155, 26–31.
Yin, A., Harrison, T.M., 2000. Geologic evolution of the Himalayan-Tibetan orogen. Annual Reviews of Earth and Planetary Science 28, 211–280.
Zeitler, P.K., Meltzer, A.S., Koons, P.O., Craw, D., Hallet, B., Chamberlin, C.P., Kidd, W.S.F., Park, S.K., Seeber, L., Bishop, M.P., Shroder, J.F., 2001. Erosion, Himalayan, geodynamics, and the geomorphology of metamorphism. Today 113, 1443–1455.